

ISSN 1450-7404

# Journal of Research in Physics

Volume 32  
Number 1  
2008



DEPARTMENT OF PHYSICS

Faculty of Sciences  
University of Novi Sad - Novi Sad - Serbia

## Indoor Radon Concentrations in Four Municipalities of the Central Part of Montenegro

Perko Vukotic<sup>1</sup>, Nevenka Antovic<sup>1</sup>, Ranko Zekic<sup>2</sup>, Ranko Svrkota<sup>3</sup>, and Radomir Ilic<sup>4</sup>

<sup>1</sup>*Faculty of Natural Sciences and Mathematics, University of Montenegro,  
81000 Podgorica, Cetinjski put b.b., Montenegro*

<sup>2</sup>*Center for Ecotoxicological Research, Podgorica, Montenegro*

<sup>3</sup>*Center for Geological Research, Podgorica, Montenegro*

<sup>4</sup>*Institute Jozef Stefan, Ljubljana, Slovenia*

Received: July 27, 2007

### Abstract

The first systematic indoor radon measurements in the central part of Montenegro were carried out in the period 2002-2003, when 280 homes in four municipalities were surveyed twice a year using CR-39 track-etch detectors, exposed each time for about six months. The annual average radon concentrations were found to be lognormally distributed ( $GM = 58.9 Bq m^{-3}$ ,  $GSD = 3.2$ ) within the range  $4 - 2,208 Bq m^{-3}$ , with an arithmetic mean of  $124 Bq m^{-3}$  and a median of  $55.4 Bq m^{-3}$ . Radon concentrations above the action level of  $400 Bq m^{-3}$  are found in 6.8% of all sampled dwellings. All these 19 locations are in detached single-family houses.

Radon concentrations were generally higher in detached single-family houses than in apartment houses, in older than in newer houses, and in rural than in urban homes. As to radon exposure indoors, this survey indicates reinforced concrete as the most favorable and stones as the most unfavorable of the building materials commonly used in Montenegro.

The average effective dose due to exposure to indoor radon in this region of Montenegro is estimated to be  $3.12 mSv y^{-1}$ , while in the rural area of the Niksic municipality, which is abundant in bauxite deposits, it amounts to  $7.31 mSv y^{-1}$ .

*Key words:*  $^{222}Rn$ , indoor, survey, detector, alpha-track, effective dose

### 1. Introduction

Radon is an inert and radioactive gas. Its three natural isotopes are produced by the decay of uranium and thorium that occur in Earth's crust. Among these isotopes,  $^{222}Rn$  is the most significant and usually called "radon". Emanating from the ground, radon gas builds up in buildings because of indoor underpressure and poor air ventilation in them. Although the ground is usually the major source of indoor radon, the other sources are building materials, water, natural gas and outdoor air.

The main reason for the growing interest in radon concentrations in homes and workplaces pertains to health: indoor radon is the main contributor to the exposure of the human population to natural sources of ionizing radiation, and one of the main causes of lung cancer. This is why many countries invest a lot of effort to make national surveys of indoor radon and identify radon-prone areas, as well as to adopt numerous related regulations. The development of the radon program in the UK is a very illustrative example of such efforts [1]. However, a recent overview of radon surveys in Europe [2] reveals clearly that the Western Balkan region is behind this trend, being characterized with scarce available data on radon.

Montenegro is one of the Western Balkan countries. It has an area of 13,812  $km^2$ , a population of 620,527, and 173,887 inhabited dwellings [3]. The radon action levels adopted in Montenegro, 400  $Bq m^{-3}$  for existing houses and 200  $Bq m^{-3}$  for future buildings, are in line with recommendations of ICRP 65 [4].

Although radon measurements in Montenegro started ten years ago [5, 6, 7, 8], the first systematic long-term radon survey commenced in 2002 within the frame of the ongoing national radon program.

As a part of this program, radon was surveyed during the period 2002-2003 in homes of the central part of Montenegro. The purpose of the survey was to obtain, for the first time, a systematic insight in the indoor radon levels in this region - to find annual average radon concentrations and estimate the related effective doses to the population, and potentially to identify houses and areas with elevated radon concentrations. This paper presents the obtained results.

## 2. Materials and Methods

### 2.1. The central part of Montenegro - demography, geology and climate

The territory of Montenegro is administratively divided into 21 municipalities, which are named after their largest towns. Four of these municipalities - Cetinje, Podgorica, Danilovgrad and Niksic, belong to the central part of Montenegro. Their total area is 4,917  $km^2$  and population 279,419, which amounts to 36 % of the area and 45 % of the population of Montenegro. Table 1 gives information on the number of inhabitants in urban and rural settlements of these four municipalities and the number of permanently inhabited dwellings, which is based on the 2003 Census [3].

**Table 1.** The number of residents and permanently inhabited dwellings in urban (U) and rural (R) settlements of the central part of Montenegro.

Municipality	Number of inhabitants		Number of dwellings	
	(U)	(R)	(U)	(R)
Cetinje	14,912	3,087	4,429	1,159
Podgorica	143,479	29,412	40,142	7,455
Danilovgrad	6,680	9,787	1,813	2,954
Niksic	56,170	16,939	14,936	4,685
total	221,241	59,225	61,320	16,253
		280,466		77,573

The central part of Montenegro belongs to the high karst geotechnical unit, whose geo-

logical structure is predominated by shallow water carbonate sediments of the Mesozoic, with the presence of Triassic volcanic rocks, Paleogene flysch sediments and Quaternary deposits [9].

The town region of Cetinje and its surroundings consists of carbonate sediments of Upper Triassic and Lower Jurassic, and Quaternary sediments. The town is situated in a typical karst field, which is made of glaciofluvial deposits up to 20 m thick. The urban settlements of Podgorica, Danilovgrad and Niksic are located in a synclinal belt, whose geological structure consists of sedimentary rocks of Triassic, Jurassic, Cretaceous, Paleocene and Quaternary age. Region of the town of Podgorica is mostly made of fluvio-glacial terrace sediments of Quaternary, up to 30 m thick, with underlying Upper Jurassic carbonate sediments. The town of Danilovgrad lies on carbonate sediments of Upper Jurassic, on lake and alluvial sediments. The town of Niksic is situated in a larger karst field, with the presence of lacustrine sediments, gravels, sands and clays (50 m thick) on carbonate bedrocks of Lower and Upper Jurassic. The area of neighboring settlements is predominantly made up of Upper Triassic dolomite and limestone, on which Jurassic red bauxite deposits were formed, which are being currently exploited. In karst depressions, where urban settlements are mainly located, soils are shallow to middle deep. In the surrounding mountains soils are poorly developed, without continuity and varying due to a dynamic relief, different bedrocks, climate and vegetation [10, 11].

In the Cetinje region, the characteristic type of soil is rendzina on limestones - crumbed, re-deposited and shallow. In the region of the town of Niksic the dominating type of soil is eutric cambisol on gravel, shallow or middle deep, while on the brink of the karst field a shallow cambic calcomelanosol is present. In the region of the town of Danilovgrad, re-deposited terra rossa and shallow terra rossa on limestones predominate, while in a wider suburban area, brown forest soil and lessive brown soil on clays and loams are present. Brown soil on fluvio-glacial deposits, shallow or deep, predominates in the region of Podgorica. Humic and rocky terra rossa, and eroded terra rossa are present on the hills.

In the central part of Montenegro the temperature, as well as the climate, varies with the altitude. The municipalities of Podgorica and Danilovgrad are in a lower area of Montenegro, practically at the sea level, and enjoy a Mediterranean climate with dry, hot summers and mild, rainy winters. The average temperature in July is about 26 °C. The absolute maximum reaches 42 °C in Podgorica, which makes it the warmest town in Montenegro. The average temperature in January is around 5 °C. The municipalities of Cetinje and Niksic, which are located in higher, mountainous areas of Montenegro, have a continental climate, with cold winters and mild summers. The average maximum temperature is 27 °C (in July - August), and average minimum temperature is -4 °C (in January).

## 2.2. Sampling

Different sampling strategies were chosen for the radon surveys in urban and in rural areas. In both cases, only dwellings with permanent occupancy were surveyed.

The sampling of urban homes was based on a regular grid covering the whole territory of the urban settlement. In each 500 m × 500 m grid square, one house was randomly selected and one dwelling within the house. Only in the town of Podgorica, the capital of Montenegro, the number of sampled homes in a square was then eventually increased depending on the density of the dwellings in that part of the town, in order to obtain a

nearly uniform sampling ratio of the whole dwelling stock in the town. The total number of urban dwellings selected in this way in the four municipalities was 198, but some of the detectors placed in these dwellings were lost during the campaign of radon measurement. Finally, the radon concentrations were obtained for 185 urban dwellings in the summer period, for 177 in the winter period, and for 172 dwellings in both of the radon measuring periods.

The sampling of rural homes was also based on a regular grid, but with  $5\text{ km} \times 5\text{ km}$  squares. One home was randomly selected in each of these 136 squares. Some of the detectors placed in the homes were lost during the campaign, so that radon concentrations were obtained for 124 rural homes in the summer period, for 115 in the winter period, and for 108 in both of the radon measuring periods.

This means that in the four municipalities of the central part of Montenegro, in total, the radon concentrations were obtained for 309 dwellings in the summer period, for 292 in the winter period, and for 280 dwellings in both of the measuring periods.

Table 2 summarizes some key data about the houses selected for radon survey, which were obtained from questionnaires.

**Table 2.** Summary of key data on radon surveyed houses ( $T^a$  = all houses,  $U^b$  = urban settlement houses,  $R^c$  = rural settlement houses).

Category		Statistics (%)														
		Whole region			Cetinje			Podgorica			Danilovgrad			Niksic		
		$T^a$	$U^b$	$R^c$	$T$	$U$	$R$	$T$	$U$	$R$	$T$	$U$	$R$	$T$	$U$	$R$
House type	Single-family detached house	79	67	98	93	82	100	75	65	100	83	75	88	77	64	97
	Multi-story apartment house	19	30	1	7	18	0	22	31	0	17	25	12	20	32	0
	One-story apartment house	2	3	1	0	0	0	3	4	0	0	0	0	3	4	3
House age	Less than 25 years old	37	45	25	24	47	8	49	53	39	33	50	25	27	30	22
	Between 25 and 40 years old	27	35	15	14	29	4	27	33	13	25	50	12	34	39	25
	Between 40 and 100 years old	28	19	42	33	12	48	17	14	25	42	0	63	38	31	50
	More than 100 years old	8	1	18	29	12	40	7	0	23	0	0	0	1	0	3
Building materials	Concrete pillars, brick walls	33	46	11	14	35	0	47	59	19	25	25	25	22	30	8
	Concrete hollow blocks	27	28	25	14	24	8	20	18	26	25	50	13	42	45	39
	Reinforced concrete	6	11	0	5	6	4	12	17	0	0	0	0	1	2	0
	Stones	34	15	64	67	35	88	21	6	55	50	25	62	35	23	53

### 2.3. Experimental

The solid-state nuclear track detectors are most suitable for the determination of the annual exposure of the general public to indoor radon [12]. The radon monitoring device of the Nuclear Center Karlsruhe (KfK) Karlsruhe [13] was found to have the best perfor-

mance among several different types of passive dosimeters employing solid-state nuclear track detectors [14], and has been successfully used in many European countries [15].

Having these facts in mind, and because of economy, it was decided to prepare and use, for nationwide long-term radon measurements, a domestically produced dosimeter which is similar to the KfK device. The schematic of this “Montenegrin” dosimeter is shown in Fig. 1. It consists of a diffusion chamber equipped with a  $25\text{ mm} \times 25\text{ mm}$  CR-39 solid-state nuclear track detector (INTERCAST, Italy) and a glass-fiber filter, which allows radon gas to enter the chamber but retains radon progeny and moisture.

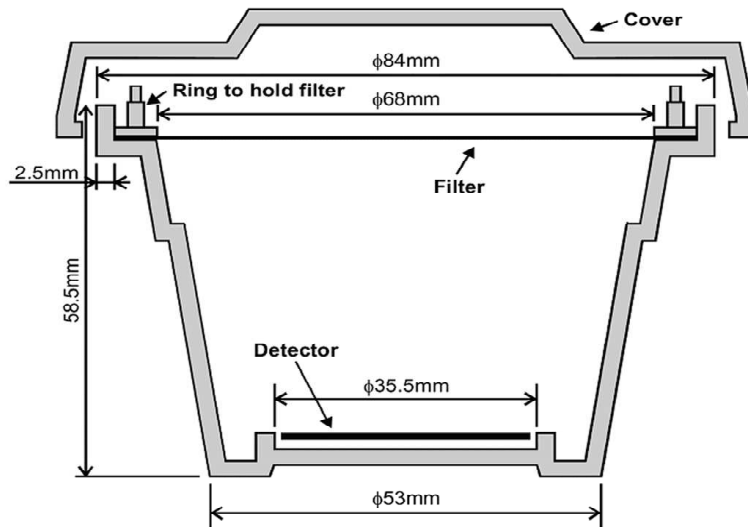


**Figure 1.** Schematic drawing of a radon dosimeter.

This dosimeter was placed in living room or bedroom on the ground floor or the first floor, in a place which is away from windows and doors, and about  $1.5\text{ m}$  above the floor and  $0.5\text{ m}$  distant from the wall. Indoor radon concentration was measured twice a year at the same place, each time during approximately six months. The detectors were exposed in the period from April to September 2002 (the “summer” period) and from October 2002 to March 2003 (the “winter” period), under normal living conditions.

In order to control the consistency and accuracy of dosimeter response, at each tenth measuring location two of our dosimeters were placed together and, again at each tenth (but another) location, a passive radon monitoring device of the J. Stefan Institute - Ljubljana, Slovenia (which is described in [16], and will be referred to as IJS radon dosimeter), utilizing a CR-39 detector, was placed beside our dosimeter.

The comparison of track densities in the paired detectors confirmed a good consistency and accuracy of the dosimeters which were used for radon measurements in Montenegro. Generally, these results were mutually consistent within a discrepancy range less than 10%, which grew to about 20% only in the cases when radon concentrations were very low.

Latent image of alpha-particle tracks in a detector foil was transformed to visible tracks with an etching technique ( $6.25\text{ M NaOH}$ ,  $70^\circ\text{C}$ , 7 hours), while track density was determined by the TRACOS automatic image analysis system [17], developed at the J. Stefan Institute - Ljubljana.

The calibration of the Montenegrin dosimeter was carried out using the radon chamber at the J. Stefan Institute. In a standard procedure [18], the response was determined as  $k_1 = 0.167 \text{ tracks cm}^{-2} \text{ Bq}^{-1} \text{ m}^3 \text{ d}^{-1}$ . Then, inter-calibration of Montenegrin dosimeters with the IJS radon dosimeter was performed - the latter being subjected to several proficiency tests in standard radon chambers in the UK. The inter-calibration gave  $k_2 = 0.165 \text{ tracks cm}^{-2} \text{ Bq}^{-1} \text{ m}^3 \text{ d}^{-1}$ . Finally, the value  $k = 0.166 \text{ tracks cm}^{-2} \text{ Bq}^{-1} \text{ m}^3 \text{ d}^{-1}$  was adopted as the arithmetic mean of the two mentioned values.

Indoor radon concentration  $C_{Rn}$  was calculated from track density  $\rho$ , using the formula

$$\rho = \rho_0 + kC_{Rn}t, \quad (1)$$

where  $t$  is the detector exposure time, and  $\rho_0$  is the background.

For an estimation of the lowest detectable radon concentration, the following formula is used

$$C_{Rn \min} = L_D (kSt)^{-1}, \quad (2)$$

where  $L_D$  is the lower limit of counted tracks for a qualitative detection, and  $S$  is the scanned area of the detector.

For a well-known blank, defined as the signal resulting from an experiment in which conditions are identical to the experiment in question, except that no radon gas is present, the definition of  $L_D$  is [19]

$$L_D = 2.71 + 3.29\sigma_B, \quad (3)$$

where  $\sigma_B$  is the standard deviation of the blank, which is defined as [20]

$$\sigma_B = \sqrt{(\rho_b + \mu_b t) \cdot S + (s \cdot S)^2}, \quad (4)$$

where  $\rho_b$  is the background track density,  $\mu_b$  is the mean rate of background radiation tracks, and  $s$  is the constant that describes variation of background track density due to variations in detector sensitivity, etching and counting technique.

In our case, an average detector exposure time was  $t = 180 \text{ d}$ , and  $\rho_b = \rho_0 = 422 \text{ tracks cm}^{-2}$ ,  $\mu_b \cong 0$ ,  $s = 2 \text{ cm}^{-2}$ ,  $S = 2.25 \text{ cm}^2$ ,  $\sigma_B \cong 31$ ,  $L_D \cong 105$ ,  $k = 0.166 \text{ tracks cm}^{-2} \text{ Bq}^{-1} \text{ m}^3 \text{ d}^{-1}$ . With these values it was obtained that  $C_{Rn \min} \cong 1.5 \text{ Bq m}^{-3}$ , which indicates a good sensitivity of the Montenegrin dosimeter.

### 3. Results

#### 3.1. Radon levels

The summary of the results obtained by indoor radon measurements in four municipalities of the central part of Montenegro is presented in Table 3 and Fig. 2.

**Table 3.** Statistics for indoor radon measurements in four municipalities of the central part of Montenegro ( $N^a$  = number of dwellings surveyed,  $AM^b$  = arithmetic mean of radon concentrations in dwellings,  $SD^c$  = standard deviation,  $GM^d$  = geometric mean,  $GSD^e$  = geometric standard deviation,  $MIN^f$  = minimum measured radon concentration,  $MAX^g$  = maximum measured radon concentration).

Municipality	$N^a$	$AM^b$ $Bq\ m^{-3}$	$SD^c$ $Bq\ m^{-3}$	$GM^d$ $Bq\ m^{-3}$	$GSD^e$	$MIN^f$ $Bq\ m^{-3}$	$MAX^g$ $Bq\ m^{-3}$	Median $Bq\ m^{-3}$
Summer period								
Cetinje	47	95.7	121	54.1	2.8	8	504	52.5
Podgorica	145	47.1	64.5	26.9	2.8	2	551	25.0
Danilovgrad	14	118	171	57.0	3.3	10	595	53.6
Niksic	103	142	214	70.1	3.2	6	1,423	66.2
whole region	309	89.3	149	43.5	3.2	2	1,423	36.8
Winter period								
Cetinje	45	130	185	76.3	2.8	9	1,178	92.6
Podgorica	137	113	176	51.8	3.4	$\leq 1.5$	1,108	50.0
Danilovgrad	12	207	237	115	3.1	23	711	102
Niksic	98	217	397	87.0	3.8	3	2,992	78.1
whole region	292	154	277	66.7	3.5	$\leq 1.5$	2,992	65.4
Annual average								
Cetinje	42	117	141	73.4	2.6	17	803	81.8
Podgorica	134	79.2	114	42.3	3.0	4	829	39.6
Danilovgrad	12	170	173	100	3.1	19	557	89.0
Niksic	92	187	301	89.0	3.3	10	2,208	74.4
whole region	280	124	206	58.9	3.2	4	2,208	55.4

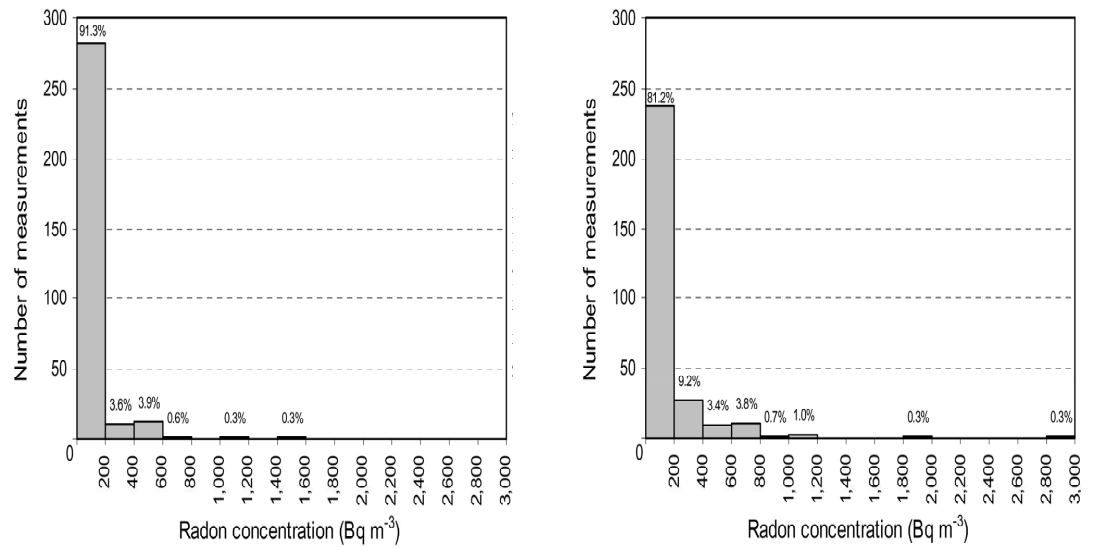


**Figure 2.1.** Diagrams of indoor radon concentrations in the central part of Montenegro:

a) summer period (309 dwellings)

b) winter period (292 dwellings).

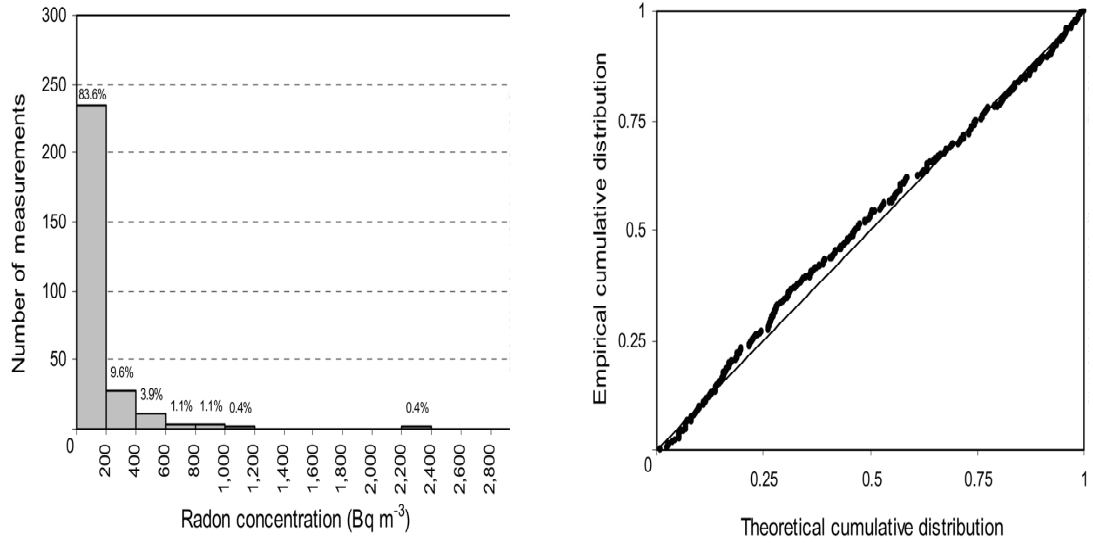


**Figure 2.2.** Diagrams of indoor radon concentrations in the central part of Montenegro:

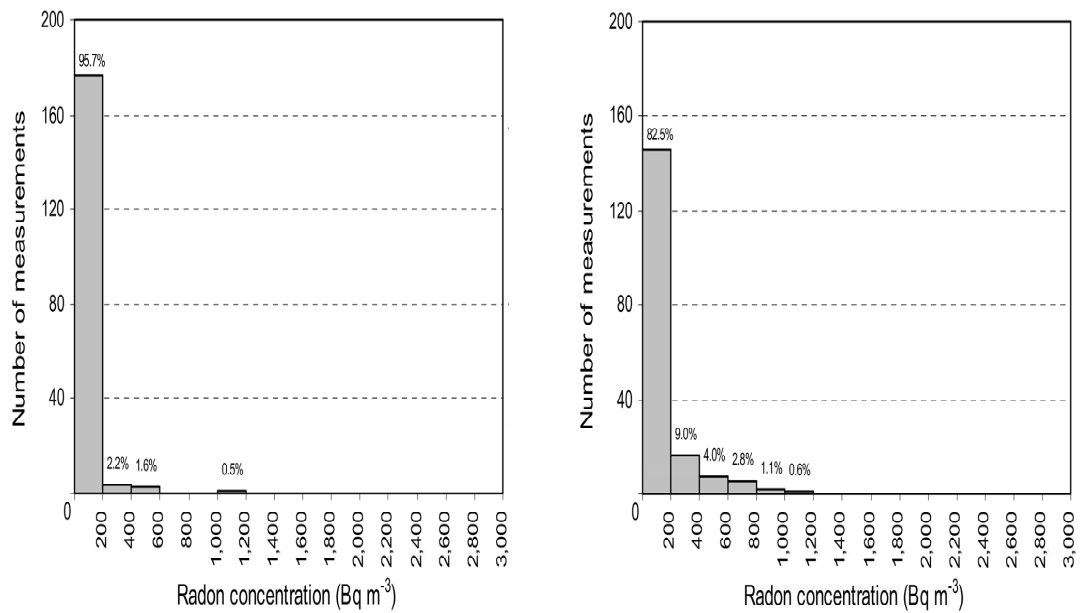
c) annual average (280 dwellings)

d) probability-probability plot (for lognormal distribution  $\mu = 4.108$ ,  $s = 1.158$ ).

Statistics for radon measurements in urban homes in this region is given in Table 4 and Fig. 3, while the same for rural homes is presented in Table 5 and Fig. 4.

**Table 4.** Statistics for radon measurements in urban homes.

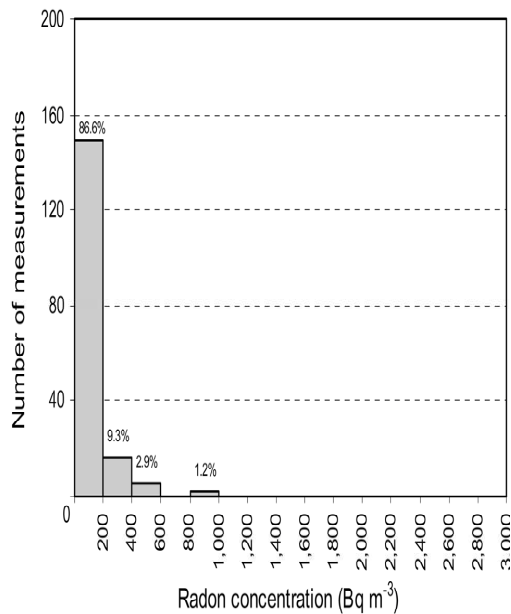
Municipality	$N$	$AM$ $Bq m^{-3}$	$SD$ $Bq m^{-3}$	$GM$ $Bq m^{-3}$	$GSD$	$MIN$ $Bq m^{-3}$	$MAX$ $Bq m^{-3}$	Median $Bq m^{-3}$
Summer period								
Cetinje	18	54.7	82.0	34.1	2.4	8	369	32.4
Podgorica	100	43.3	67.9	24.0	2.8	3	551	22.9
Danilovgrad	4	66.9	66.8	46.0	2.7	15	164	44.4
Niksic	63	98.1	161	51.0	2.9	6	1,092	42.8
whole region	185	63.6	112	32.6	2.9	3	1,092	32.0
Winter period								
Cetinje	18	100	102	65.7	2.6	16	438	92.3
Podgorica	96	122	193	51.4	3.5	5	1,108	43.9
Danilovgrad	4	147	194	79.9	3.4	23	437	64.9
Niksic	59	136	186	67.6	3.3	5	839	63.1
whole region	177	125	183	58.9	3.4	5	1,108	55.6
Annual average								
Cetinje	17	75.5	90.9	50.9	2.3	17	404	52.7
Podgorica	95	82.2	126	39.7	3.2	6	829	34.3
Danilovgrad	4	107	130	64.2	3.1	19	300	54.6
Niksic	56	121	166	65.3	2.9	10	965	61.0
whole region	172	94.8	138	48.4	3.1	6	965	42.8



**Figure 3.1.** Frequency distribution of radon concentrations in urban homes of the central part of Montenegro:

a) summer period (185 dwellings)

b) winter period (177 dwellings).

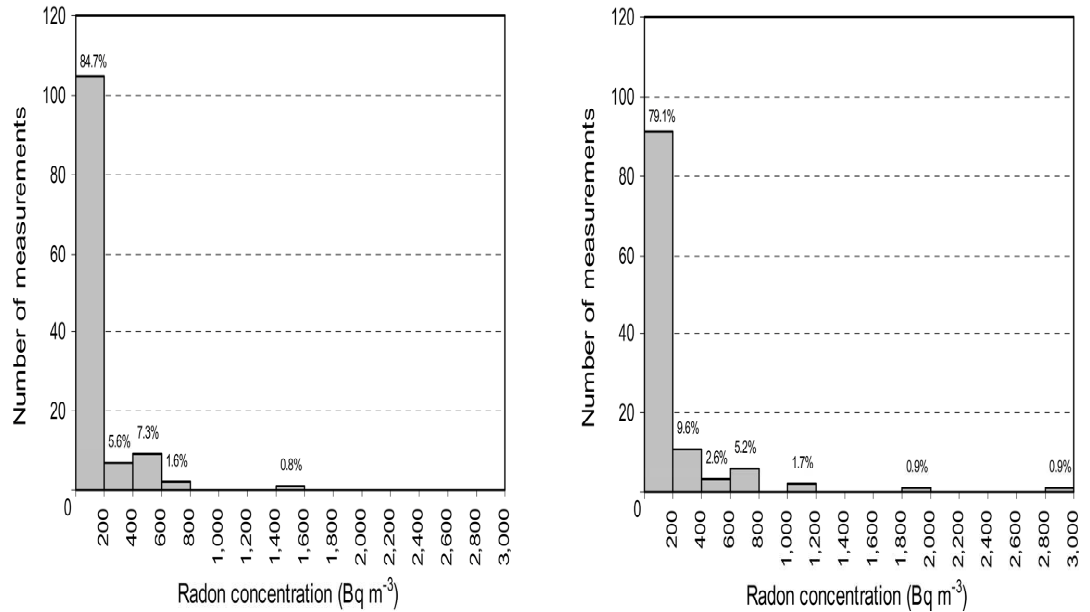


**Figure 3.2.** Frequency distribution of radon concentrations in urban homes of the central part of Montenegro:

c) annual average (172 dwellings).

**Table 5.** Statistics for radon measurements in rural homes.

Municipality	$N$	$AM$ $Bq\ m^{-3}$	$SD$ $Bq\ m^{-3}$	$GM$ $Bq\ m^{-3}$	$GSD$	$MIN$ $Bq\ m^{-3}$	$MAX$ $Bq\ m^{-3}$	Median $Bq\ m^{-3}$
Summer period								
Cetinje	29	121	136	72.0	2.8	14	504	81.0
Podgorica	45	55.8	55.8	34.8	2.8	2	260	32.2
Danilovgrad	10	138	198	62.0	3.7	10	595	53.6
Niksic	40	210	265	116	3.1	9	1,423	110
whole region	124	128	186	63.6	3.3	2	1,423	61.4
Winter period								
Cetinje	27	150	224	84.3	2.9	9	1,178	92.6
Podgorica	41	90.5	125	52.4	3.0	$\leq 1.5$	767	56.0
Danilovgrad	8	237	263	138	3.1	25	711	133
Niksic	39	338	569	127	4.5	3	2,992	127
whole region	115	199	375	84.7	3.6	$\leq 1.5$	2,992	83.4
Annual average								
Cetinje	25	145	162	94.0	2.6	19	803	99.5
Podgorica	39	71.8	79.2	49.2	2.4	4	478	48.1
Danilovgrad	8	201	191	126	3.0	19	557	96.9
Niksic	36	290	417	144	3.4	18	2,208	141
whole region	108	171	276	87.6	3.1	4	2,208	86.2

**Figure 4.1.** Frequency distribution of radon concentrations in rural homes of the central part of Montenegro:

a) summer period (124 dwellings)

b) winter period (115 dwellings)

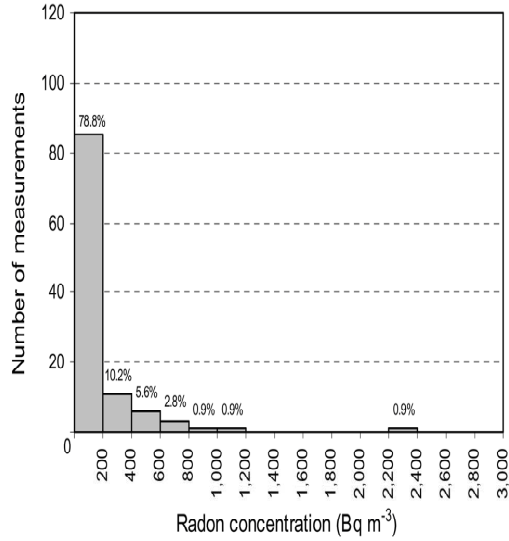


**Figure 4.2.** Frequency distribution of radon concentrations in rural homes of the central part of Montenegro:

c) annual average (108 dwellings).

Table 6 gives the arithmetic mean and median of annual radon concentrations in dwellings classified by house type, age and building material.

**Table 6.** The arithmetic mean (*AM*) and median of annual radon concentrations in dwellings depending on house type, age and building material.

Category	Classification	<i>AM</i> ( $Bq\ m^{-3}$ )	Median ( $Bq\ m^{-3}$ )
House type	Single-family detached house	144.3	74.6
	Apartment house	48.9	18.5
House age	Less than 25 years old	76.9	45.6
	More than 25 years old	152.2	63.6
Building materials	Concrete pillars and brick walls	91.6	50.5
	Concrete hollow blocks	93.6	44.1
	Reinforced concrete	21.2	14.7
	Stones	203.2	97.6

### 3.2. Effective doses

On base of the results for radon concentrations, the average annual effective doses to the general public, which result from a continued exposure to radon at home, can be estimated using the dose calculation model given in [21]. That model uses a conversion convention for radon exposure based on the equality of detriments from epidemiological determinations. Adopting the equilibrium factor of 0.4 and values of occupancy time and dose coefficient as those used in [21], the effective dose was calculated as follows

$$C_{Rn} [Bq m^{-3} \times 0.4 \times 7000 [h] \times 9 [nSv (Bq h m^{-3})^{-1}]], \quad (5)$$

where  $C_{Rn}$  is the arithmetic mean of indoor radon concentrations. The doses in the central part of Montenegro, calculated by the expression (2), are given in Table 7.

**Table 7.** Effective doses from domestic radon in the central part of Montenegro.

Municipality	Average effective dose ( $mSv y^{-1}$ )		
	all homes	urban homes	rural homes
Cetinje	2.95	1.91	3.65
Podgorica	2.00	2.07	1.81
Danilovgrad	4.28	2.70	5.06
Niksic	4.71	3.05	7.31
whole region	3.12	2.39	4.31

The world average annual effective dose due to radon indoors, calculated in the same way by [21], is  $1.0 mSv$ .

#### 4. Discussion

Fig. 2d clearly shows that the distribution of annual average concentrations of indoor radon in the central part of Montenegro is approximately lognormal (with  $GM = 58.9 Bq m^{-3}$  and  $GSD = 3.2$ ), which is in accordance with general findings for dwellings worldwide [21].

The average annual radon level in homes of the central part of Montenegro, given in Table 3 ( $AM = 124 Bq m^{-3}$ ,  $GM = 58.9 Bq m^{-3}$ ), is significantly higher than the worldwide average:  $AM = 40 Bq m^{-3}$ ,  $GM = 30 Bq m^{-3}$  [21]. The arithmetic mean value of annual radon concentration in dwellings for eight countries of Southern Europe, the region Montenegro belongs too, ranges from  $7 Bq m^{-3}$  (Cyprus) to  $120 Bq m^{-3}$  (Albania), with an average value of  $68 Bq m^{-3}$  [21]. This means that the average indoor radon level in the central part of Montenegro is at the upper edge of that range, practically the same as in neighboring Albania, i.e. almost twice higher than the South European average.

As Fig. 2 shows, annual indoor radon concentrations were mostly (83.6%) below  $200 Bq m^{-3}$ . Concentrations between  $200 Bq m^{-3}$  and  $400 Bq m^{-3}$  were found at 27 locations (9.6% of all sampled dwellings).

There were 19 locations (6.8% of all sampled dwellings) with annual radon concentrations above the action level of  $400 Bq m^{-3}$  - 11 of them with radon concentrations in the range of  $400 - 600 Bq m^{-3}$ , three in the range of  $600 - 800 Bq m^{-3}$ , three in the range of  $800 - 1,000 Bq m^{-3}$ , one with  $1,185 Bq m^{-3}$ , and one with the highest radon level of  $2,208 Bq m^{-3}$ . With respect to their geographical position, two of them belong to the Cetinje municipality, three to Podgorica, one to Danilovgrad and 13 to the Niksic municipality. This means that indoor radon concentrations higher than action level were found in 4.8% of all sampled dwellings in the Cetinje municipality, 2.2% in Podgorica, 8.3% in Danilovgrad, and even 14.1% in the Niksic municipality. While the statistics in the case of Danilovgrad is very poor (only 12 dwellings sampled) and the corresponding result should be taken with precaution, the statistics evidently indicate the Niksic municipality

as a radon prone area, which is mainly a consequence of the bauxite deposits in this region, with a uranium content of  $4 - 14 \mu\text{g g}^{-1}$  [8]. All of these 19 locations are on ground floors in detached single-family houses (16 of them are one-story and three are two-story houses), and 16 of them are rural homes. It is indicative that those houses are relatively old (12 are older than 50 years, and only two were built after 1980), and mostly built of stones or a combination of stones and concrete (13 of them). Six of them are without or with very thin concrete slabs in the basement.

Tables 4 and 5 reveal that radon concentrations in rural homes are generally higher than in urban homes: on the average twice higher in the summer period, about 50% higher in the winter period, and with about an 80% higher annual average of indoor radon. Again, the Niksic region has the highest annual radon concentrations in rural homes ( $AM = 290 \text{ Bq m}^{-3}$ ,  $GM = 144 \text{ Bq m}^{-3}$ ), while Podgorica has the lowest ( $AM = 71.8 \text{ Bq m}^{-3}$ ,  $GM = 49.2 \text{ Bq m}^{-3}$ ).

As expected, the radon concentrations in the winter period were significantly higher than in the summer months (about 70% higher comparing AM and median values in Table 3).

Table 7 shows that the average effective dose for the population in the central part of Montenegro due to radon in homes is more than three times higher than the worldwide average of  $1.0 \text{ mSv y}^{-1}$  [21]. The lowest average effective dose is found in urban homes of the Podgorica municipality ( $1.91 \text{ mSv y}^{-1}$ ), and the highest in the rural homes of the Niksic region, where the average dose is more than seven times above the worldwide average.

Results presented in Table 6 support a generally known fact that radon concentrations are higher in detached single-family houses than in apartment buildings, and show that, as to radon exposure indoors, reinforced concrete is far the best among building materials commonly used in Montenegro, while the stones are far the worst. From Table 6 it is also evident that radon levels are lower in newer houses, which are built with modern building materials and with thicker concrete slabs in basements.

The results of this radon survey can be compared with some previous radon measurements in the town of Podgorica [6] and in the Niksic region [8], which were carried out with cellulose nitrate track detectors exposed for about 90 days in winter season 1994/1995. Then, an arithmetic mean of radon concentrations in 110 dwellings in the town of Podgorica was found to be  $77.4 \text{ Bq m}^{-3}$ , median  $52.8 \text{ Bq m}^{-3}$ , and there was 1.8% of dwellings with radon concentrations above the action level (in this work, in Table 4, the corresponding values are  $122 \text{ Bq m}^{-3}$ ,  $43.9 \text{ Bq m}^{-3}$  and 6.2% respectively), while in the Niksic region, the arithmetic mean for 15 dwellings was  $230 \text{ Bq m}^{-3}$  and 13.3% of dwellings were with radon above the action level (in this work, in Table 3, these values are  $217 \text{ Bq m}^{-3}$  and 15.3% respectively).

#### 4. Conclusions

The average annual radon concentration in homes in four municipalities of the central part of Montenegro ( $AM = 124 \text{ Bq m}^{-3}$ ,  $GM = 58.9 \text{ Bq m}^{-3}$ ) is significantly above the worldwide average. The average indoor radon level in this part of Montenegro is almost twice higher than the South European average.

Radon concentrations are found to be generally higher in detached single-family houses than in apartment houses, in older than in newer houses, and in rural than in urban homes. All 19 locations where radon levels above the action level of  $400 \text{ Bq m}^{-3}$  were

found (6.8% of all 280 sampled dwellings) are in detached single-family houses. As to radon exposure indoors, reinforced concrete appears as the most favorable and stones as the most unfavorable of the building materials commonly used in Montenegro.

The average effective dose for the local population of this region due to exposure to radon indoors is estimated to be  $3.12 \text{ mSv y}^{-1}$ , while in the rural area of the Niksic municipality, which is abundant in bauxite deposits, it amounts to  $7.31 \text{ mSv y}^{-1}$ .

### Acknowledgments

This study was performed within the national program of indoor radon survey in Montenegro, which was funded by the Ministry of Environment and organized by the Center for Ecotoxicological Research (CER), Podgorica. The authors wish to thank I. Kobal (J. Stefan Institute, Slovenia), for his kind help in carrying out calibration of the radon dosimeters, and the staff of the CER and students at the Department of Physics of the University of Montenegro for valuable assistance in the field measurements.

### References

1. G. M. Kendall, B. M. R. Green, J. C. H. Miles, D. W. Dixon, *J. Radiol. Prot.* **25**, 475 (2005).
2. G. Dubois, "An overview of radon surveys in Europe", EUR 21892 EN, European Communities (2005).
3. MONSTAT, "Census of Population, Households and Dwellings in the Republic of Montenegro in 2003", Statistical Office of the Republic of Montenegro, Podgorica (2005) (in Serbian).
4. International Commission on Radiological Protection, "Protection against radon-222 at home and at work", Oxford: Pergamon Press, ICRP Publication 65 (1993).
5. V. V. Uvarov, V. M. Kulakov, P. Vukotic, S. Dapchevic, N. Saveljic, I. Picuric, A. M. Marennny, A. S. Voroztsov, N. A. Nefedov, N. Antovic, Rare gas geochemistry - applications in earth & environmental sciences (H. S. Virk, ed.) - Proceedings of the 3rd International colloquium on rare gas geochemistry, Amritsar, India, December 1995, p. 283-291 (1997).
6. P. Vukotic, S. Dapchevic, N. Saveljic, V. V. Uvarov, V. M. Kulakov, *Radiat. Meas.* **28**, 755 (1997).
7. P. Vukotic, G. I. Borisov, V. V. Kuzmich, N. Antovic, S. Dapchevic, V. V. Uvarov, V. M. Kulakov, *J. Radioanal. Nucl. Chem.* **235**, 151 (1998).
8. N. Antovich, V. V. Uvarov, P. Vukotich, S. Dapchevich, *Geofis. Int.* **41**, 321 (2002).
9. M. Mirkovic, M. Zivaljevic, V. Djokic, Z. Perovic, M. Kalezic, M. Pajovic, "Geological Map of Montenegro, 1:200,000 scale", Center for Geological Research, Podgorica, Montenegro (1985) (in Serbian).
10. G. Djuretic, B. Fustic, M. Djuretic, P. Celebic, "Pedological Map of SFR Yugoslavia, 1:50,000 scale", Agricultural Institute, Titograd (1965, 1966, 1970, 1986) (in Serbian).

11. B. Fustic, G. Djuretic, *Soils of Montenegro*, (University of Montenegro, Podgorica, 2000) (in Serbian).
12. A. C. George, *Health Phys.* **70**, 451 (1996).
13. M. Urban, E. Piesch, *Radiat. Prot. Dosimetry* **1**, 97 (1981).
14. K. Jamil, K. K. Al-Ahmady, F. Rehman, S. Ali, A. A. Qureshi, H. A. Khan, *Health Phys.* **73**, 629 (1997).
15. L. W. Put, J. Lembrechts, E. R. van der Graaf., P. Stoop, *Health Phys.* **78**, 94 (2000).
16. M. Humar, T. Sutej, J. Skvarc, L. Mljac, M. Radez, R. Ilic, *Radiat. Prot. Dosimetry* **45**, 549 (1992).
17. J. Skvarc, *Informacije MIDEM* **23**, 205 (1993).
18. T. Sutej, R. Ilic, M. Najzer, *Nucl. Tracks Radiat. Meas.* **15**, 547 (1988).
19. R. Ilic, J. Rant, T. Sutej, E. Kristof, J. Skvarc, M. Kozelj, M. Najzer, M. Humar, M. Cercek, B. Glumac, B. Cvikl, A. Fajgelj, T. Gyergyek, A. Trkov, A. Loose, J. Peternelj, J. Remec, M. Ravnik, *Nucl. Tracks Radiat. Meas.* **17**, 483 (1990).
20. R. Ilic, J. Rant, *Nucl. Tracks Radiat. Meas.* **19**, 619 (1991).
21. United Nations Scientific Committee on the Effects of Atomic Radiation, "Sources and Effects of Ionizing Radiation", Report to the General Assembly of the United Nations with Scientific Annexes, New York - United Nations (2000).

## Elimination of Parasitic Effects in the Measurement of Electrical Properties of High-resistance Chalcogenide Semiconductors

Miloš P. Slankamenac<sup>1</sup>, Svetlana R. Lukić<sup>2</sup>, Miloš Živanov<sup>1</sup>

<sup>1</sup>*University of Novi Sad, Faculty of Technical Sciences, Novi Sad,*

<sup>2</sup>*Institute of Physics, Faculty of Sciences and Mathematics, University of Novi Sad,  
Trg Dositeja Obradovića 4, 21000 Novi Sad, Serbia*

Received: April 9, 2008

### Abstract

In this paper is presented a method for electrical characterization of the high-resistance semiconductor  $Ge_{20}As_{14}S_{28}Se_{28}I_{10}$  in bulk form using Impedance/Gain - Phase Analyzer HP 4149A and High-resistance meter HP 4329A instruments. The problems of parasitic effects during measurements of some parameters are discussed in detail. Measurement methods, experimental setups, and calculation methods for the elimination of the influence of parasitic effects on measured values are presented.

*Key words:* Electrical parameters, parasitic effects, semiconductor, chalcogenide

### 1. Introduction

The applications of chalcogenide glasses include energy management, thermography, temperature monitoring, electronic circuit detection, laser technique and IR-spectroscopy, as well as high-resolution optics in night image technique. As an example, the blackbody radiation emitted by room temperature objects such as the human body is situated in the range of  $8 \div 12 \mu m$ , where selenide telluride based glasses are applicable for thermal imaging [1]. Other optical applications are based on the high refractive index of the chalcogenide glasses. They exploit the increase of the transmission of coatings with decreased reflection. These glasses are used as antireflection coating for IR filters. Depending on the composition, one can change continuously the refractive index of these glasses from the values around  $n = 2$  for non-stoichiometric arsenic sulfide with large excess of sulfur up to  $n = 3.5$  for the systems with tellurium [2, 3].

With the exception of optical fibers the thin-film waveguides are fundamental media for the integrated optics. On the basis of them is studied the construction of the devices for introducing, processing and extraction of the information and transmission at various distances.

The thin-film planar waveguides consist of dielectric layers whose refractive index is higher than that of the substrate and the other layer. This ensures the use of the total reflection phenomenon for directing light without losses. At the same time we must

have low losses ( $\sim 1dB/cm$ ). Losses as low as  $0.4dB/cm$  were obtained for the case of  $As_{40}Se_{10}S_{40}Ge_{10}$  amorphous composition [4]. High optical transparency of both film and substrate and the absence of high scattering must be ensured for a good waveguide. The most interesting wavelength range for laser communication lines is VIS, near IR and the radiation of  $10.6\mu m$  of the  $CO_2$  laser used for processing and transmission of signals of the laser locators.

Every material has a unique structure and appropriate electrical and dielectrical properties. Accurate measurements of these properties enable one to get important information about material under test. Based on these data, production processes are controlled, quality is improved and material or electrical component is adjusted to a certain purpose.

## 2. Experimental details

Systems for measuring electrical and dielectrical properties of materials, electrical components and devices usually consist of impedance or network analyzer, with test fixture for connecting an instrument to the tested sample and the computer. The computer is connected with the instrument and has the appropriate software for transferring, storing, displaying and later processing measured values (Fig. 1).

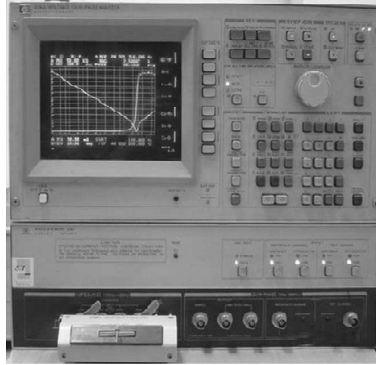


**Figure 1.** Impedance/Gain - Phase Analyzer HP 4149A.

A type of test fixtures depends on the chosen measurement technique and physical properties of the tested sample. The most frequently used techniques are: parallel plate, coaxial probe, transmission line, resonant cavity and free-space.

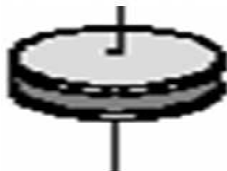


**Figure 2.** A principle of making and appearance of the sample.

The parallel-plate method is one of the most utilizable, precise and simple methods for measuring electrical and dielectrical properties of the sample. Fig. 2 shows the principle of this method, which is based on the capacitor form of tested sample, and appearance of the final sample with silver electrodes. During AC (alternate current) measurements [5], DC (direct current) measurements are performed [6] at various temperatures in order to acquire all relevant parameters of the sample (Fig. 3).



**Figure 3.** DC measurements at various temperatures.

Measurements last relatively long (three to four hours per sample) and mostly depend on the number of temperature points. After achieving desirable temperature on the sample holder in the temperature chamber, you should wait about ten minutes for the transition processes to be finished and the sample to be heated to a desirable temperature.

During AC (alternate current) measurement [5], DC (direct current) measurement is performed [6] on various temperatures in order to acquire all relevant parameters of the sample (Fig. 3). Measurements last relatively long (three to four hours per sample) and mostly depend on the number of temperature points. After achieving a desired temperature on the sample holder in the temperature chamber, one should wait for about ten minutes for the transition processes to be finished and the sample to be heated to that temperature.

### 2.1. Parasitic Effects on Measurement

During measurements of DC and AC electrical parameters of high-resistance materials, there are some difficulties due to parasitic effects and a limited degree of the instruments' accuracy. During DC electrical resistance measurement, it is very important to use instruments with wide scale of measurements of high resistance and low current. High resistance meter HP 4329A, which measures electrical resistance from  $500\text{ k}\Omega$  to  $2 \cdot 10^{16}\ \Omega$  and current from  $pA$  to  $\mu A$ , are presented in Fig. 3. The principle of measurement of this instrument is based on bringing adjustable and known DC voltage (test voltage) to sample electrodes and measuring current by precise pico-ammeter simultaneously. During these measurements it is necessary to know the break voltage of the sample, to avoid damaging the sample. Voltage is adjustable in range of  $10\text{ V}$  to  $1000\text{ V}$ , better measurement accuracy being obtained at higher voltages. When test voltage is adjusted it is useful to know the degrees of nonlinearity of the sample so as to get more accurate analyses of the measured parameters later.

During electrical DC measurements of high resistance materials in the temperature chamber, it is necessary to connect its metal shell with the ground of the instrument. A great problem can make static electricity in the measurement room caused by the proximity of people and their clothes.

During electrical AC measurements of high resistance materials in the temperature chamber, it is necessary to take into account test fixtures and temperature chambers

impacts on the measurements. When measurements are performed at room temperature by a test fixture or a probe, the HP 4149A instrument has the possibility of compensating for their impacts by an open-short method. This method of compensation is performed by measuring open and short parameters of the test fixture or the probe parameters. The instrument uses these parameters for later mathematical elimination of test fixtures and chamber temperature impacts.

There are two types of open-short compensation: compensation at all measurement points (all points method) and compensation with average measurement values (interpolation method).

## 2.2. Elimination of Parasitic Effects

Parallel connection between a capacitor and a resistor is the best model of high resistance materials between two electrodes during electrical properties measurement (Fig. 4) [7].

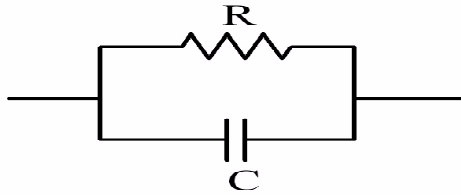


**Figure 4.** Model of high-resistance materials.

The HP 4194A instrument measures an impedance  $R + jX$  in the mode of serial equivalent circuit and admittance  $G + jB$  in the mode of parallel equivalent circuit as a function of frequency. Other parameters are calculated from these four parameters. Values of parameters from the model shown in Fig. 4 are calculated in the following manner:

$$R = \frac{1}{G},$$

$$C = \frac{B}{\omega} = \frac{B}{2\pi f} \quad (1)$$

When measurements of electrical properties are performed at different temperatures, there are impacts of test fixtures and temperature chamber on parasitic effect of measured values.

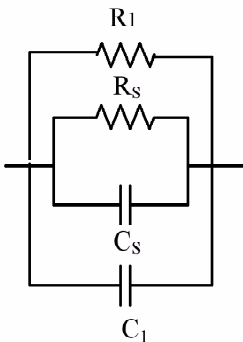


**Figure 5.** Model of high-resistance component with parasitic effects.

The temperature chamber is designed to work from  $77\text{ K}$  to  $430\text{ K}$  so it has relatively large dimensions, because of the space for liquid nitrogen. The lengths of wires, which connect instruments with sample electrodes, are  $15\text{ cm}$  and they have impact on the measurements. Also, the sample holder, which has two parallel plates insulated mutually, has a larger area of intersection than samples. It implies the parasitic parallel capacitance  $C_1$  and resistance  $R_1$ , which are attached on an ideal model of samples (parameters  $C_s$  and  $R_s$ ), shown in Fig. 5. In an ideal case  $R_1$  has infinite resistance, whereas  $C_1$  is equal to zero. Whereas in real case for high-resistance com-

ponents,  $R_1$  at high frequencies is only one or two degrees of value higher than  $R_S$ , and  $C_1$  is one half to two degrees of value lower than  $C_S$ .

These parasitic effects could be eliminated mathematically after the measurement. It is done by measured parameters ( $C_C$  and  $R_C$ ) for open electrodes of the temperature chamber (without the sample) connected with a test fixture without internal compensation. After that, the sample parameters ( $C$  and  $R$ ) are measured together with the impact of temperature chamber and the test fixture. Since the dimensions of the sample are known ( $S = a \cdot b$  - area of intersection of the sample,  $d$  - thickness of the sample), the parameters of the sample are obtained by calculation:

$$\begin{aligned} C_S &= C - C_C + C_{S0}, \\ R_S &= \frac{R_C R}{R_C - R} \end{aligned} \quad (2)$$

where  $C_{S0} = \varepsilon_0 \frac{S}{d}$  is the capacitance of the air capacitor with the area and thickness of the sample.

Electrical properties of amorphous semiconductors [8] are very interesting and have been investigated for many years [9, 10]. Table 1 shows the measured and compensated parameters of the capacitances as a function of frequency for high-resistance amorphous semiconductor glass  $Ge_{20}As_{14}S_{28}Se_{28}I_{10}$ .

**Table 1.** Measured and compensated parameters of the capacitances.

$f (Hz)$	$C_S (F)$	$C (F)$	$C_C (F)$
100.0	$7.64 \cdot 10^{-13}$	$1.21 \cdot 10^{-12}$	$5.10 \cdot 10^{-13}$
126.6	$7.44 \cdot 10^{-13}$	$1.21 \cdot 10^{-12}$	$5.30 \cdot 10^{-13}$
160.3	$6.88 \cdot 10^{-13}$	$1.19 \cdot 10^{-12}$	$5.60 \cdot 10^{-13}$
661.4	$5.53 \cdot 10^{-13}$	$1.15 \cdot 10^{-12}$	$6.56 \cdot 10^{-13}$
837.6	$5.61 \cdot 10^{-13}$	$1.14 \cdot 10^{-12}$	$6.39 \cdot 10^{-13}$
1060.8	$5.28 \cdot 10^{-13}$	$1.13 \cdot 10^{-12}$	$6.62 \cdot 10^{-13}$
1343.3	$5.27 \cdot 10^{-13}$	$1.12 \cdot 10^{-12}$	$6.60 \cdot 10^{-13}$
7017.1	$4.54 \cdot 10^{-13}$	$1.05 \cdot 10^{-12}$	$6.63 \cdot 10^{-13}$
8886.2	$4.44 \cdot 10^{-13}$	$1.04 \cdot 10^{-12}$	$6.63 \cdot 10^{-13}$
11253.3	$4.37 \cdot 10^{-13}$	$1.03 \cdot 10^{-12}$	$6.58 \cdot 10^{-13}$
14251.2	$4.27 \cdot 10^{-13}$	$1.02 \cdot 10^{-12}$	$6.60 \cdot 10^{-13}$
58780.1	$3.93 \cdot 10^{-13}$	$9.98 \cdot 10^{-13}$	$6.67 \cdot 10^{-13}$
74438.0	$3.89 \cdot 10^{-13}$	$9.93 \cdot 10^{-13}$	$6.67 \cdot 10^{-13}$
94266.8	$3.84 \cdot 10^{-13}$	$9.89 \cdot 10^{-13}$	$6.68 \cdot 10^{-13}$
492388.2	$3.60 \cdot 10^{-13}$	$9.64 \cdot 10^{-13}$	$6.67 \cdot 10^{-13}$
623550.7	$3.57 \cdot 10^{-13}$	$9.61 \cdot 10^{-13}$	$6.67 \cdot 10^{-13}$
789652.3	$3.54 \cdot 10^{-13}$	$9.57 \cdot 10^{-13}$	$6.66 \cdot 10^{-13}$
1000000.0	$3.50 \cdot 10^{-13}$	$9.53 \cdot 10^{-13}$	$6.65 \cdot 10^{-13}$

Frequency points are selected from the logarithmic allocation of the scale from 100 to 1000000  $Hz$ . Measurements have been done at room temperature (300  $K$ ). The dimensions

of the sample are  $S = 14 \text{ mm}^2$  and  $d = 1.97 \text{ mm}$ , so that the calculated value of the capacitance is  $C_{S0} = 6.27 \cdot 10^{-14} \text{ F}$ .

Fig. 6 shows the capacitances of the sample  $\text{Ge}_{20}\text{As}_{14}\text{S}_{28}\text{Se}_{28}\text{I}_{10}$  as a function of frequency.

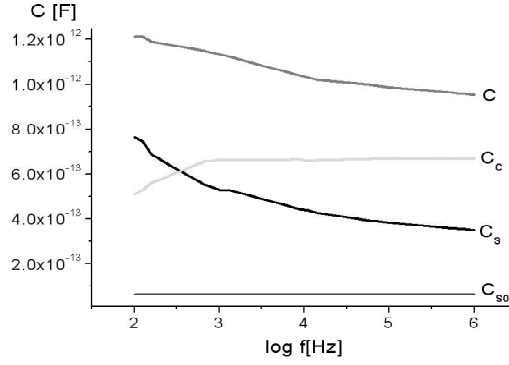


**Figure 6.** Capacitances of the sample  $\text{Ge}_{20}\text{As}_{14}\text{S}_{28}\text{Se}_{28}\text{I}_{10}$  as a function of frequency.

It can be noticed that the measured capacitance  $C$  is larger than the capacitance of the sample  $C_S$  for the approximate value of  $5 \cdot 10^{-13} \text{ F}$ . The capacitances decrease with the increase of frequency, which is evident from Fig. 6. At lower frequencies (from  $100 \text{ Hz}$  to  $1 \text{ kHz}$ )  $C_S$  has a more pronounced drop than  $C$ , whereas at higher frequencies they have approximately the same slopes. This may be explained by smaller capacitance values of the chamber  $C_C$  at lower frequencies, because of the higher impact of an inductive component. The inductive component derives itself from inductivity of the wire conductors, which connect the sample and the instrument.

**Table 2.** Measured and compensated parameters of resistance.

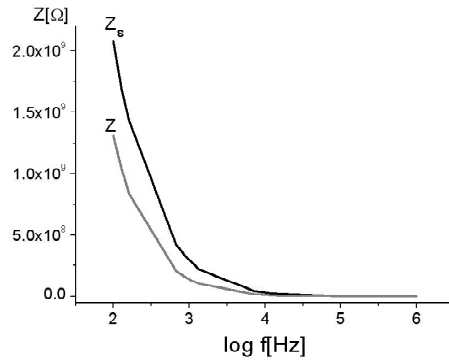
$f \text{ (Hz)}$	$R_S \text{ (}\Omega\text{)}$	$R \text{ (}\Omega\text{)}$	$R_C \text{ (}\Omega\text{)}$
100.0	$3.06 \cdot 10^{10}$	$2.90 \cdot 10^{10}$	$5.66 \cdot 10^{11}$
126.6	$2.42 \cdot 10^{10}$	$2.30 \cdot 10^{10}$	$4.66 \cdot 10^{11}$
160.3	$1.46 \cdot 10^{10}$	$1.40 \cdot 10^{10}$	$3.66 \cdot 10^{11}$
661.4	$2.26 \cdot 10^9$	$2.20 \cdot 10^9$	$7.99 \cdot 10^{10}$
837.6	$1.74 \cdot 10^9$	$1.70 \cdot 10^9$	$7.89 \cdot 10^{10}$
1060.8	$1.48 \cdot 10^9$	$1.45 \cdot 10^9$	$6.26 \cdot 10^{10}$
1343.3	$1.13 \cdot 10^9$	$1.11 \cdot 10^9$	$5.75 \cdot 10^{10}$
7017.1	$3.43 \cdot 10^8$	$3.37 \cdot 10^8$	$1.98 \cdot 10^{10}$
8886.2	$2.91 \cdot 10^8$	$2.85 \cdot 10^8$	$1.48 \cdot 10^{10}$
11253.3	$2.36 \cdot 10^8$	$2.31 \cdot 10^8$	$1.23 \cdot 10^{10}$
14251.2	$1.98 \cdot 10^8$	$1.94 \cdot 10^8$	$1.01 \cdot 10^{10}$
58780.1	$7.63 \cdot 10^7$	$7.53 \cdot 10^7$	$5.66 \cdot 10^9$
74438.0	$6.42 \cdot 10^7$	$6.30 \cdot 10^7$	$3.37 \cdot 10^9$
94266.8	$5.44 \cdot 10^7$	$5.25 \cdot 10^7$	$1.55 \cdot 10^9$
492388.2	$1.30 \cdot 10^7$	$1.09 \cdot 10^7$	$6.75 \cdot 10^7$
623550.7	$1.03 \cdot 10^7$	$8.25 \cdot 10^6$	$4.21 \cdot 10^7$
789652.3	$8.06 \cdot 10^6$	$6.21 \cdot 10^6$	$2.71 \cdot 10^7$
1000000.0	$6.17 \cdot 10^6$	$4.62 \cdot 10^6$	$1.84 \cdot 10^7$

Table 2 shows the measured and compensated parameters of the resistance as a function of frequency for the  $Ge_{20}As_{14}S_{28}Se_{28}I_{10}$  sample. It is evident that the resistance of the sample  $R_S$  is larger than the measured values of the resistance in the chamber. The difference between these two values is about 5%. In order to investigate the impact of the presence of the parasitic effects caused by the temperature chamber and the test fixture on some electrical [11] and dielectric properties [12] of the sample, we will consider the measurement results of the impedance and dielectric permittivity of the sample with and without compensation.

These parameters are calculated in the following way:

$$\begin{aligned} Z &= \frac{1}{\sqrt{G^2 + B^2}} = \frac{1}{\sqrt{\frac{1}{R^2} + (2\pi fC)^2}}, \\ \varepsilon' &= \frac{C}{C_0} \end{aligned} \quad (3)$$

Fig. 7 presents the curves of the sample impedances with ( $Z_S$ ) and without the compensation ( $Z$ ) as a function of frequency. Because of the parasitic effects, the impedance measured without compensation is lower than by the compensation. Both the increase in the effective capacitance and decrease in the effective parallel resistance affect the decrease of the impedance, which is evident from the formula (3).



**Figure 7.** Impedances of the sample  $Ge_{20}As_{14}S_{28}Se_{28}I_{10}$  as a function of frequency.

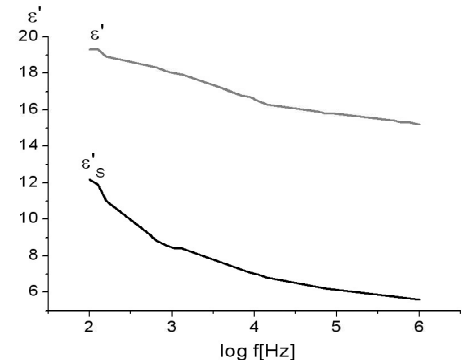


**Figure 8.** Dielectric permittivities of the sample  $Ge_{20}As_{14}S_{28}Se_{28}I_{10}$  as a function of frequency.

Fig. 8 shows the curves of the sample dielectric permittivity with ( $\varepsilon'_S$ ) and without the compensation ( $\varepsilon'$ ) as a function of frequency. Because of the parasitic effects, the measured dielectric permittivities without compensation are significantly higher than the values obtained by the compensation.

### 3. Conclusion

Based on theoretical analysis and experimental AC measurements by HP 4149A instrument, it can be concluded that there is significant impact of parallel parasitic capacitances and resistance during the measurement of electrical properties of highly resistant samples. These parasitic effects are the consequences of inevitable impacts of test fixtures and

temperature chamber (its wires and sample holder which is not ideal). It has been demonstrated that the impact of parasitic capacitances is higher than of parasitic resistance. Also, it has been shown that parasitic effects have more impact on dielectrical permittivity than on impedance. Relatively simple mathematical method for compensation impacts of parasitic effects has been proposed and the results of measurements for the amorphous semiconductor glass sample  $Ge_{20}As_{14}S_{28}Se_{28}I_{10}$  have been shown.

### Acknowledgments

This work was supported by the Provincial Sekretariat of Science and Tehnological Development, Autonomous Province of Vojvodina, Project “Tehnology of obtaining and characterization of disordered semiconductors”.

### References

1. R.B. Johnson, in Proc. Soc. Photo-Optical Instrumentation Engineers (SPIE) **915**, 106 (1988) .
2. Z. Cimpl, F. Kosek, Phys. Stat. Sol. (a) **93**, K55 (1986).
3. Z. Cimpl, F. Kosek, J. Non-Cryst. Solids **90**, 577 (1987).
4. S. Zembutsu, S. Fukunishi, Appl. Optics **18**, 393 (1989).
5. Miloš Slankamenac, Svetlana R. Lukić, Electrical Conductivity of Chalcogenide Glassy Semiconductors of the  $Cu - As - Se - I$  System, *Symposium of Industrial Electronics*, Banja Luka, Bosnia and Herzegovina, pp. 20-22 (2006).
6. Miloš P. Slankamenac, Svetlana R. Lukić, Fedor Skuban, Imre O. Gut, Miloš Živanov, J. Res. Phys. **31(1)**, 61 (2007).
7. N. F. Mott, E. A. Davis, *Electronic processes in Noncrystalline materials*, (Clarendon press, Oxford, 1971).
8. S. Lukić, D. Petrović, *Complex noncrystalline chalcogenides*, (University of Novi Sad, Faculty of Sciences, Novi Sad, 2002).
9. M. Popescu, Disordered chalcogenide optoelectronic materials: phenomena and applications, J. Optoelectron. Adv. Mater. **7(4)**, 2189 (2005).
10. Miloš P. Slankamenac, Svetlana R. Lukić, Miloš B. Živanov, Electrical switching effects in the chalcogenide glassy semiconductor  $Cu_5(A_SSe_{1.4}I_{0.2})_{95}$  (article in press), *ReCIMiCO workshop*, Novi Sad, Serbia (2008).
11. Miloš Slankamenac, Miloš Živanov, Svetlana R. Lukić, Fedor Skuban, Energija, ekonomija, ekologija **10(3)**, 59 (2008).
12. Dalibor Sekulić, Miloš Slankamenac, Miloš Živanov, Tehnika - Novi Materijali, **17(3)**, 6 (2008).

## DSC and XRD Analysis of Inclusion Complexes of Pharmacologically Active Compounds

A. Kapor , S. Skuban , V. Nikolić , Ž. Cvejić\* , S. Rakić  
*Department of Physics, Faculty of Sciences, University of Novi Sad,  
Trg Dositeja Obradovića 4, 21000 Novi Sad, Serbia,  
e-mail: akapor@uns.ns.ac.yu*

*\*Faculty of Technology, University of Niš, Bulevar oslobođenja 124, 16000 Leskovac,  
Serbia,  
e-mail: nvesna@yahoo.com*

Received: July 4, 2008

### Abstract

The inclusion complexes are a special group of the so-called “non-classical complexes. The components of the inclusion complexes are the “host” and “guest” molecules. The “host” molecules are compounds that in their crystal structure, or in their aggregates, have large enough cavities into which the molecules of the other component (“guest” molecules) can be enclosed. Here we present the procedure of the identification of inclusion compounds consisting of the comparative study of DSC and XRD records of the active “guest” compound (atenolol, amlodipine and nifedipine), the “host” compound ( $\beta$ -cyclodextrin and its derivative 2-hydroxypropyl- $\beta$ -cyclodextrin) and their inclusion complexes, which are also compared with the physical mixture of these substances. This procedure of comparing DSC and XRD results has proved to be sufficiently reliable for confirming the inclusion, at least in the case when the “host” compound was  $\beta$ -cyclodextrin and its derivative.

*Key words:* Inclusion complexes,  $\beta$ - cyclodextrin, DSC and XRD records, comparative study

### 1. Introduction

The use of complexation of different drugs with cyclodextrins (CDs) has been extensively studied in recent years, with the aim of improving definite characteristics of pharmaceutical interest, such a solubility in aqueous media, dissolution rate, chemical stability and bioavailability [1]. This procedure has been evaluated for several series of pharmacologically active compounds. Careful determinations of the stoichiometry of the inclusion reported different stoichiometry for the same compound in many cases.

Cyclodextrins (CDs) are cyclic oligosaccharides with the ability to encapsulate entirely, or at least partially, into their hydrophobic cavity, a wide variety of “guest” molecules, forming inclusion complexes [2]. Many cyclodextrin complexes are stored as dried crystals

in contact with the atmosphere and therefore under variable conditions. It is of practical interest to understand the interaction of such materials with the atmosphere [3] and inclusion of water molecules into the crystalline structure of cyclodextrin, in order to understand the mechanism of the inclusion of pharmacologically active small molecule into the molecule of CDs, mostly  $\beta$ -CD.  $\beta$ -CD hydrate is an impressive example of a solid in which fast diffusion of water molecules is possible without the presence of permanent diffusion channels. It must be assumed that the observed long-range mobility is made possible by positional fluctuations of the  $\beta$ -CD atoms, whereby bottlenecks between neighboring asymmetric crystal units are temporarily opened [3].

## 2. Materials

The inclusion of the active “guest” molecule into the crystalline lattice of cyclodextrin ( $\beta$ -CD) and 2-hydroxypropyl- $\beta$ -cyclodextrin (2-HP- $\beta$ -CD) will be considered in terms of the example of formation of three groups of inclusion complexes with active compounds atenolol, amlodipine and nifedipine.

Atenolol is the  $\beta$ -blocker with low solubility in aqueous gastric fluids [4]. Industrially, atenolol is produced as a racemic mixture of the two enantiomers. Both forms are bioactive in treating hypertension, angine and arrhythmia, which makes it a truly versatile drug [5].

The antihypertensive drug substance amlodipine besylate crystallizes in two stable crystalline forms: an anhydrate and monohydrate [6]. The anhydrous form is used in our investigation. Amlodipine besylate is a long-acting calcium channel blocker used as an antihypertensive and in the treatment of angina [7]. Nifedipine is a highly photolabile practically water-insoluble drug used therapeutically as a calcium channel antagonist for the treatment of various cardiovascular disorders [8, 9]. Poor and erratic bioavailability is observed following oral administration of crystalline nifedipine, mostly due to its low aqueous solubility and slow dissolution rate within the gastrointestinal tract [10].

I group of studied complexes with active compound atenolol has two complexation attempts:

Ia -atenolol (AT) and  $\beta$ -cyclodextrin ( $\beta$ -CD)

Ib -atenolol and 2-hydroxypropyl- $\beta$ -cyclodextrin (2-HP- $\beta$ -CD)

II group of studied complexes with active compound amlodipine was also complexed with both compounds of cyclodextrin as “host” molecules.

IIa -amlodipine (AMLO) and  $\beta$ -cyclodextrin ( $\beta$ -CD)

IIb -amlodipine and 2-hydroxypropyl- $\beta$ -cyclodextrin (2-HP- $\beta$ -CD)

III group of studied compounds is an attempt of complexation of nifedipine (NF) with  $\beta$ -cyclodextrin ( $\beta$ -CD).

## 3. Experimental details

Preparation of inclusion complex by co-precipitation, and reparation of physical mixture was the same in all three groups of materials [11]. The compounds were studied in

the same manner. The initial active compounds, “host” compound, their synthesized inclusion complexes as well as the physical mixtures of “host” and “guest” compounds were examined by the methods of differential scanning calorimetry (DSC) and X-ray powder diffraction (XRD).

DSC plots were recorded at DuPont DSC instrument with heating rate of  $10^{\circ}\text{C}/\text{min}$  within the temperature range from  $303 - 553\text{ K}$  in I and II group of compounds and from  $303 - 603\text{ K}$  in III group of compounds with nifedipine which has higher decomposition temperature.

XRD plots were recorded at the automatic powder diffractometer PHILIPS PW1030 with  $\text{CuK}\alpha$  radiation in the angular range  $2\theta = 5 - 65^{\circ}$  with step of  $0.05^{\circ}$  and exposition time  $5\text{ s}$ .

#### 4. Results and Discussion

Comparative recording of DSC spectra are presented in Figs. 1-3. Analyzing the peaks, it was noticed that samples of active “guest” compounds possess expressed endothermic peaks which define their melting point. Values obtained are: atenolol  $428\text{ K}$ , amlodipine  $474\text{ K}$  and nifedipine  $446\text{ K}$  which agree well with previously determined values [4, 6, 8].

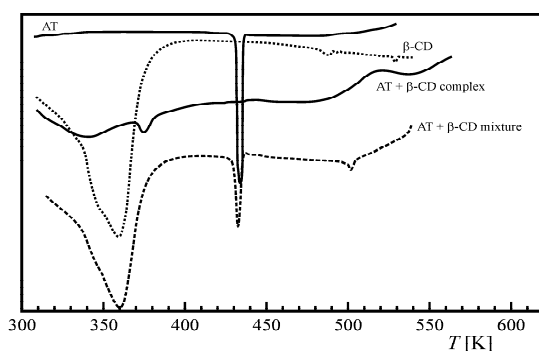


**Figure 1.a.** DSC curves: atenolol (AT) and  $\beta$ -cyclodextrin ( $\beta$ -CD)

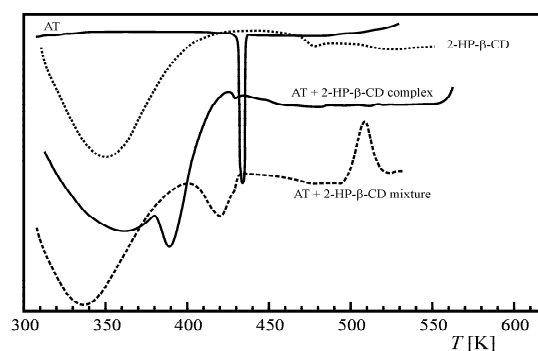


**Figure 1.b.** DSC curves: atenolol (AT) and 2-hydroxypropyl- $\beta$ -cyclodextrin (2-HP- $\beta$ -CD)

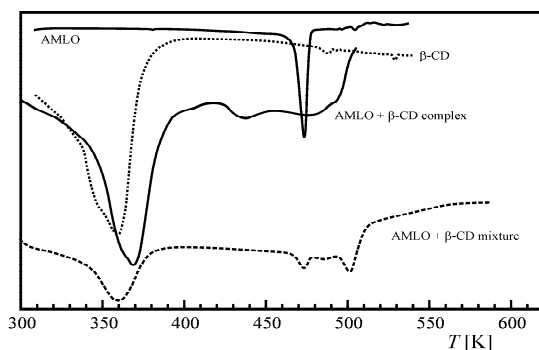


**Figure 2.a.** DSC curves: amlodipine (AMLO) and  $\beta$ -cyclodextrin ( $\beta$ -CD)

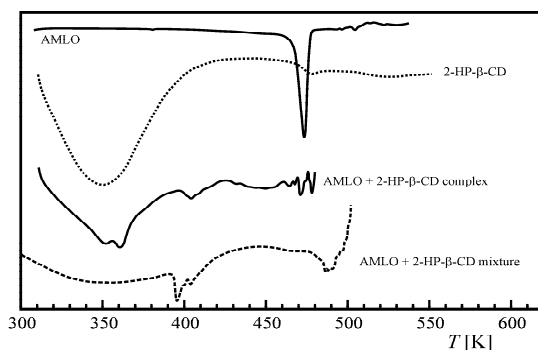


**Figure 2.b.** DSC curves: amlodipine (AMLO) and 2-hydroxypropyl- $\beta$ -cyclodextrin (2-HP- $\beta$ -CD)

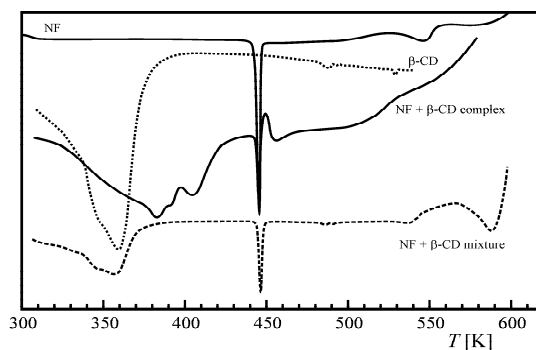


**Figure 3.** DSC curves: nifedipine (NF) and  $\beta$ -cyclodextrin ( $\beta$ -CD)

Since the inclusion of “guest” molecule into the “host” molecules leads to the loss of physical identity of “guest” molecule [3], one expects that if the complex is formed, its DSC plot either does not possess at all, or possesses weakly present characteristic endothermal peak which determines the melting point of the “guest” compound.

The comparative analysis of all three groups of compounds, allows us to conclude that atenolol and amlodipin successfully complex with  $\beta$ -cyclodextrin and 2-hydroxypropyl- $\beta$ -cyclodextrin, while nifedipine remains uncomplexed and most probably forms a binary mixture.

The other part of the analysis which should confirm the results of DSC plots was recording the powder diffractograms of the same compounds. Comparative diffractograms for all three groups of compounds are given in Fig. 4-6.

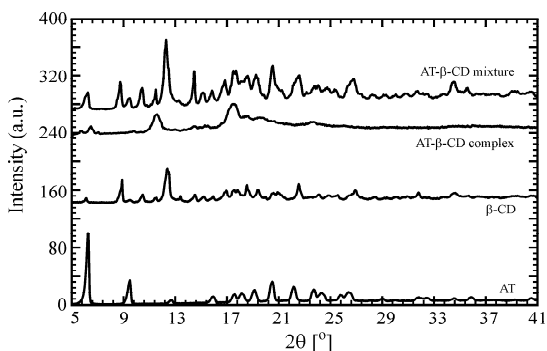


**Figure 4.a.** XRD plots: atenolol (AT) and  $\beta$ -cyclodextrin ( $\beta$ -CD)

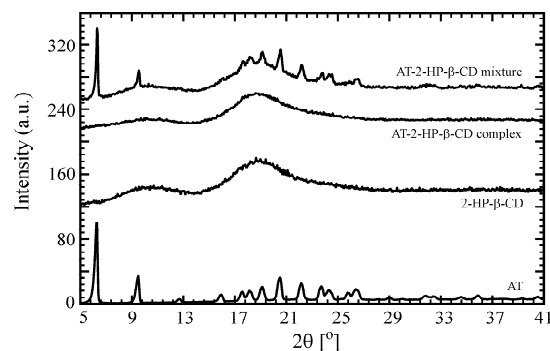


**Figure 4.b.** XRD plots: atenolol (AT) and 2-hydroxypropyl- $\beta$ -cyclodextrin (2-HP- $\beta$ -CD)

Since powder diffractogram reflects the dimensions and symmetry of the unit cell of the crystalline lattice of the powder compound, as well as the absence of peaks in the case of amorphous compound, one expects that in the case of formation of the inclusion complex, its diffractogram corresponds to the diffractogram of “host” compound,  $\beta$ -cyclodextrin ( $\beta$ -CD) and 2-hydroxypropyl- $\beta$ -cyclodextrin (2-HP- $\beta$ -CD) in our case. Additional indication is the comparison of diffractograms of the formed inclusion complex and the physical mixture of “guest” and “host” compounds. If these diffractograms differ, we can talk

about partial or total complexation by the inclusion of “guest” molecule into the “host” molecules.

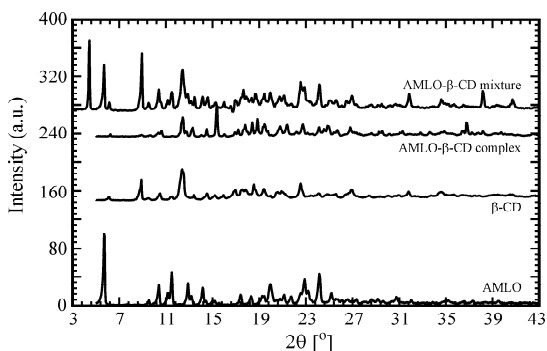


**Figure 5.a.** XRD plots: amlodipine (AMLO) and  $\beta$ -cyclodextrin ( $\beta$ -CD)

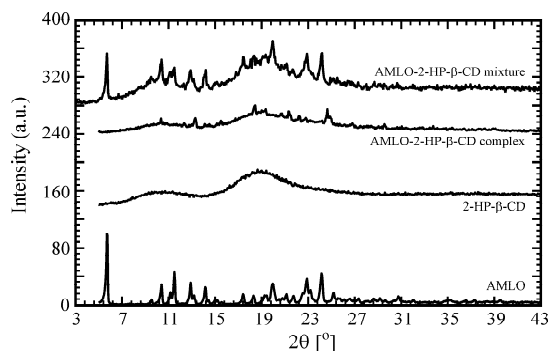


**Figure 5.b.** XRD plots: amlodipine (AMLO) and 2-hydroxypropyl- $\beta$ -cyclodextrin (2-HP- $\beta$ -CD)

The analysis of Fig. 4.a, and Fig. 5.a indicates the substantial difference in XRD plots of complexes and physical mixtures. The analysis of XRD plots of the physical mixture shows that the powder possesses two phases so that maxima correspond to the positions of maxima obtained by recording the individual samples of “guest” and “host” compounds. This tells us about the simultaneous presence of both compounds in the crystalline state.

In the case of complexation of the active compound with 2-hydroxypropyl- $\beta$ -cyclodextrin (2-HP- $\beta$ -CD), it turned out that this cyclodextrin derivative is amorphous, with two characteristic peaks ( $2\theta = 10.5^\circ$  and  $18.9^\circ$  Fig. 4.b, 5.b). XRD plot of the complex with this compound confirmed the inclusion of the active “guest” molecule into the crystalline lattice of the “host”, since it retained the characteristic XRD plot of the “host”, in this case it is 2-hydroxypropyl- $\beta$ -cyclodextrin (2-HP- $\beta$ -CD). The additional sharp peaks in Fig. 5.b. indicate that the inclusion was only partial since they point to the presence of non-included “guest” compound.

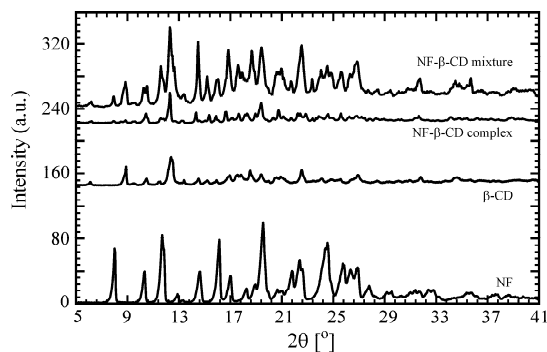


**Figure 6.** XRD plots: nifedipine (NF) and  $\beta$ -cyclodextrin ( $\beta$ -CD)

In the case of nifedipine as the “guest” molecule, expressed peaks indicate high crys-

tallinity of both “guest” and “host” compounds as well as complex and physical mixture. One can not notice any major difference between the XRD plots of inclusion complex and physical mixture (Fig. 6). One can not claim with certainty the formation of inclusion complex. Since the results of DSC analysis also arise some doubts into the formation of inclusion complex, the analysis of XRD plots, confirms them. However, on the basis of XRD plots, one can not exclude the possibility of the partial inclusion of the molecule. There are indications to that direction by some previous studies [8], showing the influence of heating the physical mixtures of varying molar ratios and suggesting that inclusion complexation is not the dominant mechanism, but rather monomolecular dispersion of nifedipine within the cyclodextrin matrix.

## 5. Conclusion

The aim of this study was to indicate to the possibility of the application of two rather simple analytical methods for comparatively quick testing of the formation of inclusion complexes between pharmacologically active “guest” compound and its “host”,  $\beta$ -cyclodextrin and 2-hydroxypropyl- $\beta$ -cyclodextrin. On the other hand, the confirmation of complexing with  $\beta$ -cyclodextrin is extremely important in the pharmaceutical industry since it implies the production of products with much higher solubility in the water, increasing the bioavailability of the active component and consequently the total therapeutic effect. One of the expected effects of decreasing the concentration of the active component is the decrease of drug side effects.

Good knowledge of the thermal and crystallographic properties of “host” compounds, in our case primarily  $\beta$ -cyclodextrin enables simplified analysis of DSC and XRD plots of potential inclusion complexes with various biologically active molecules.

## Acknowledgments

This work was supported by Ministry of Science of the Republic of Serbia Project No. 142059.

## References

1. K. H. Frömring, J. Szejtli (Eds.) *Cyclodextrins in Pharmacy*, (Kluwer, Dordrecht, 1994.).
2. W. Saenger, *Angew. Chem. Int. Ed. Engl.* **19**, 344 (1980).
3. T. Steiner, G. Koellner, *J. Am. Chem. Soc.* **116**, 5122 (1994).
4. R. Ficarra, P. Ficarra, M. R. Di Bella, D. Raneri, S. Tommasini, M. L. Calabro, M. C. Gamberini, C. Rustichelli, *J. Pharm. Biomed. Anal.* **23**, 33 (2000).
5. E. Paroli, *Farmacologia Clinica Tossicologia*, (Universo, Roma, 1995.).
6. J. M. Rollinger, A. Burger, *J. Therm. Anal. Cal.* **68**, 361 (2002).
7. Martindale, *The Extra Pharmacopoeia*, (Royal Pharmaceutical Society, 1999).
8. M. E. Brown, B. D. Glass, M. S. Worthington, *J. Therm. Anal. Cal.* **68**, 631 (2002).

9. E. M. Sorkin, S. P. Clissold, S.P.Brogden, *Drugs* **30**, 182 (1985).
10. S. L. Ali, In: *Analytical Profiles of Drug Substances*, Ed.: K. Florey, (Academic Press Inc., New York, 1989).
11. V. Nikolić, Lj. Nikolić, M. Stanković, A. Kapor, M. Popsavin, D. Cvetković. *J. Serb. Chem. Soc.* **72**, 737-746 (2007).

## The Possibility of the Application of Planar Scintillation Detector for Muon Hodoscopy

N. Jovančević, J. Papuga, G. Šoti, N. Todorović, J. Slivka, M. Vesković, M. Krmar,  
S. Forkapić, I. Bikit

*Department of Physics, Faculty of Sciences, University of Novi Sad,  
Trg Dositeja Obradovića 4, 21000 Novi Sad, Serbia*

Received: November 20, 2008

### Abstract

The possibility of the application of a planar scintillation detector for muon hodoscopy was investigated. This would allow us to determine the rate of muons of various angles on a given energy in the experimental spectrum. Simulations of the passage of muons through the scintillation detector were carried out in GEANT4. Beams of muons were generated with different energy and different incident angle. The system was calibrated and the angular resolution was determined. The results of the simulation were compared with the experimental ones.

*Key words:* Planar scintillation detector, muon hodoscopy, Geant4 simulation toolkit

### 1. Introduction

Muons are the main component of cosmic rays at sea level. They are generated in collisions of the primary particles with atoms of the atmosphere. We can identify them by the scintillation which they induce when passing through the detector. These scintillations result from the ionization and excitation of atoms in the detector.

In this paper we investigate the possibility of the application of planar scintillation detector for muon hodoscopy. A hodoscope is a device which shows the path of a charged particle. We started with the supposition that the deposited energy of muons in the detector depends of the initial angles, which allows us to determine the count rate of muons at various angles on a given energy in the experimental spectrum.

Simulations of the passage of muons through the scintillation detector were carried out in GEANT4. Beams of muons were generated with different energy (from 1 GeV to 20 GeV in different steps) and different incident angle (from 0° to 80° in steps of 10°). The results of simulations were compared with the experimental ones.

The application of a scintillation detector for muon hodoscopy is a new and a simple method. The fact that we do not have to use complex detector system (wire chambers,

coincidental detectors) makes this method attractive and promising for future research.

## 2. Description of the experiment and the simulation

The experimental spectrum was obtained by the plastic scintillation detector placed on the ground-floor of the Department of Physics building. The detector (type SCIONIX) had dimensions  $0.5\text{ m} \times 0.5\text{ m} \times 0.05\text{ m}$ , and it was made of polystyrene as scintillation material. The total time of measuring was  $t = 1531989\text{ s}$ .

Simulations of the passage of muons through the scintillation detector were carried out in GEANT4 [1],[2]. The  $0.05\text{ m}$  thick plastic scintillator, installed at the Department of Physics, was modeled. The incident angle of the muon beam (with 100,000 muons per beam) varied from  $0^\circ$  to  $80^\circ$  in steps of  $10^\circ$ . The muon energy varied from 1 to  $20\text{ GeV}$ .

When muons pass through the detector, they lose part of their energy and excite the detector's atoms. When those atoms deexcite, they emit optical photons. This process is called scintillation and the energy lost by muons is the deposited energy. The deposited energy maximum in the given spectrum is called the peak of the deposited energy.

The total loss energy for muons can be expressed by the following relation

$$-\frac{dE}{dx} = a(E) + b(E)E \quad (1)$$

where  $a(E)$  represents the energy loss due to ionization and atomic excitation. It has a weak logarithmic energy dependence and it sometimes appears as constant;  $b(E)$  represents the energy loss due to bremsstrahlung, pair production and photo-nuclear interactions [3]. For relativistic particle (charge  $Z \cdot e$ ) the term  $a(E)$  can be given by the Bethe-Bloch formula:

$$-\frac{dE}{dx} = 4\pi N_a r_e^2 m_e c^2 \frac{Z}{A} \frac{1}{\beta^2} \left[ \ln \left( \frac{2m_e c^2 \gamma \beta^2}{I} \right) - \beta^2 - \frac{\delta}{2} \right] \quad (2)$$

where  $Z$  and  $A$  are atomic number and atomic weight of the detector material;  $m_e$  is the electron rest mass;  $r_e$  is the classical radius of the electron;  $\gamma = \frac{1}{\sqrt{1-\beta^2}}$  is the Lorentz factor;  $\beta = \frac{v}{c}$  is the velocity of the particle and  $c$  is the velocity of light;  $I$  is ionization constant (approximately given by  $16 Z^{0.9}\text{ eV}$  for  $Z > 1$ );  $dx$  is the mass per unit area;  $\delta$  is the density effect [3].

## 3. Results and Discussion

The obtained results are presented in Table 1. It shows how the peak of the deposited energy (in  $\text{MeV}$ ) varies with the energy of the muons and with the incident angle.

Based on these results we can conclude that the variation of peak of the deposited energy is less than 5% in a column, therefore in the following sections only  $2\text{ GeV}$  muons are considered. We can also conclude that the deposited energy depends strongly on the incident angle. The decrease of the incident angle will shift the peak towards smaller energies. This is consistent with the theoretical expectations, because if we increase the incident angle, the path of particles through the detector will increase too.

**Table 1.** The peak of the deposited energy.

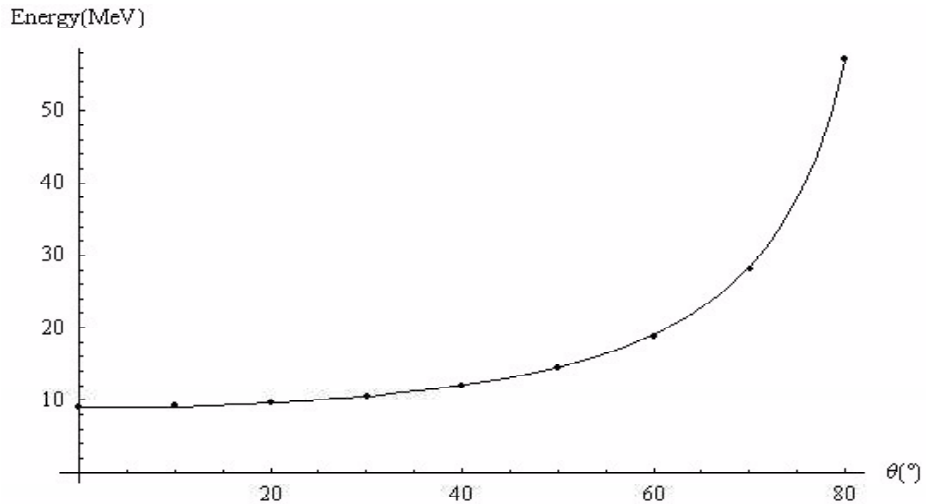
Muon energy [GeV]	Incident angle $\Theta$ [°]								
	0	10	20	30	40	50	60	70	80
1.0	8.9	9.1	9.7	11.9	14.4	18.6	27.6	57.1	57.1
1.5	9.1	9.2	9.5	10.5	11.8	14.5	18.5	27.7	57.8
2.0	9.2	9.3	9.7	10.5	12.1	14.3	18.7	28.3	56.7
2.5	9.1	9.2	9.7	10.7	12.1	14.6	19.1	28.3	57.3
3.0	9.1	9.3	9.7	10.7	12.1	14.5	18.9	28.1	57.1
5.0	9.3	9.1	9.8	10.6	11.9	14.5	18.8	28.0	57.2
7.0	9.2	9.2	9.9	10.6	12.0	14.4	19.0	27.8	56.4
10.0	9.3	9.4	9.7	10.8	12.0	14.5	18.8	28.1	57.7
20.0	9.3	9.4	9.9	10.8	12.0	14.6	19.4	28.7	57.2

This function is given by the next relationship:

$$E \propto \frac{dE}{dx} \frac{d}{\cos \Theta} = \frac{c}{\cos \Theta}$$

where  $\frac{dE}{dx}$  represents the differential energy loss;  $d$  - thickness of the detector;  $\Theta$  represents the incident angle and  $c = \frac{dE}{dx} \cdot d$  is constant.

By fitting the results from Table 1, we obtain the function  $E = E(\Theta)$ , which is presented in Figure 1.

**Figure 1.** The peak of the deposited energy as a function of the incident angle.

The fit function has the form  $f(\Theta) = a \cdot \frac{1}{\cos \Theta} + b$ , with the coefficients  $a = 10.09(4)$  and  $b = -1.13(10)$ , and  $r^2 = 0.999$ . These coefficients can be used in the future experiments.

The effect of shifting of the deposited energy peak toward a higher energy with increase in the initial angle is shown in Figure 2. There are two spectra illustrated. For muons

with an incident angle of  $\Theta = 10^\circ$ , the peak of the deposited energy is at  $9.3 \text{ MeV}$  and for  $\Theta = 70^\circ$  the peak is at  $28.3 \text{ MeV}$ .

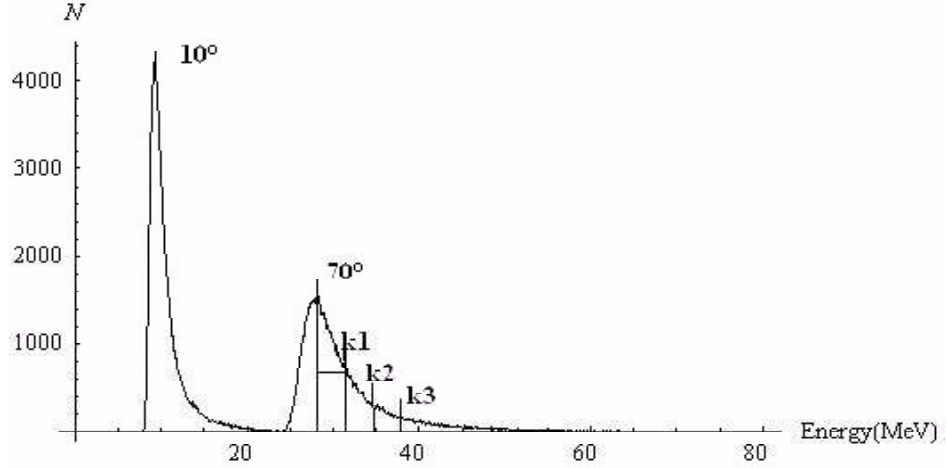


**Figure 2.** The displacement of the two spectra ( $\Theta = 10^\circ$  and  $\Theta = 70^\circ$ ).

It can be seen from Figure 2. that the spectra have different HWHM. In order to check whether the shapes of these two spectra are the same, we constructed the rate coefficients  $k_i = \frac{N(i \cdot HWHM)}{N_{peak}}$ , where  $N(i \cdot HWHM)$  represents the count at the energy which is increased by  $i$  ( $i = 1, 2, 3$ ) multiplied by HWHM;  $N_{peak}$  represents the counts at the peak.

**Table 2.** The rate coefficients.

$k$	Incident angle $\Theta$ [ $^\circ$ ]								
	0	10	20	30	40	50	60	70	80
$k_1$	0.515	0.508	0.510	0.534	0.510	0.518	0.511	0.501	0.494
$k_2$	0.246	0.262	0.233	0.231	0.247	0.221	0.231	0.198	0.180
$k_3$	0.131	0.133	0.113	0.114	0.138	0.110	0.107	0.114	0.110

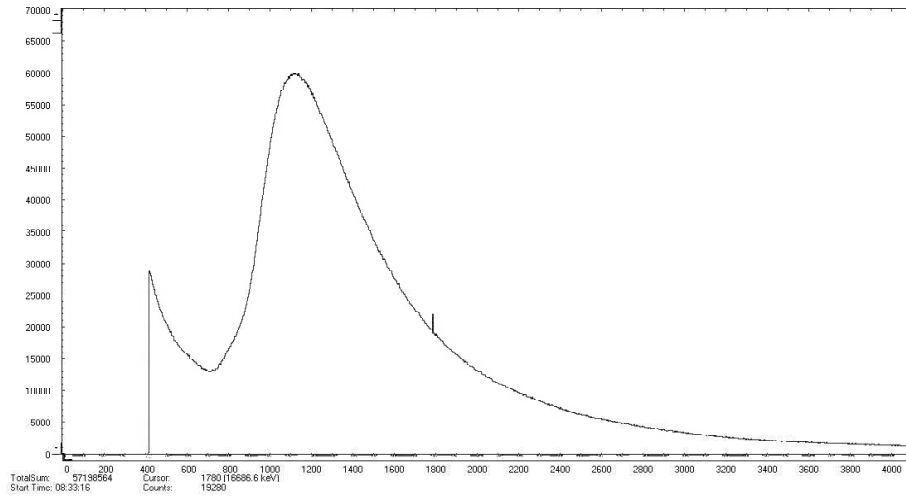
We can see from the values presented in Table 2 that the rate coefficients for a given  $i$  are the same for different incident angles. Thus we come to the conclusion that the simulated spectra have the same shapes.

The peak of the deposited energy of the muons with the same initial angle is not ideally narrow. Thus in the sum spectrum of all simulations some of the peaks overlap. In these cases we can not determine the incident angle of the muons precisely. Since we know from Table 2 that the peak shapes are the same for muons of different incident angles, we can calculate the influence of those muons. Table 3 presents the calculated results based on the simulations.

**Table 3.** The simulation results.

$\Theta$ [ $^{\circ}$ ]	Count rate ( $\Theta$ )	Count rate ( $\Theta - 10^{\circ}$ )	Count rate ( $\Theta - 20^{\circ}$ )	Count rate ( $\Theta - 30^{\circ}$ )
0	100 %	X	X	X
10	56 %	44 %	X	X
20	41 %	35 %	24 %	X
30	34 %	30 %	25 %	11 %
40	40 %	30 %	17 %	13 %
50	62 %	23 %	15 %	0
60	64 %	36%	0	0
70	78%	22%	0	0

The experimentally obtained spectrum of muons is shown in Figure 3. The peak of the muon energy is approximately at 10 MeV, which is in agreement with the simulation and with the fact that the most of the muons have small incident angle. The experimental spectrum contains angles from  $0^{\circ}$  to  $70^{\circ}$ . This spectrum was divided into the areas which included the angle intervals from  $0^{\circ}$  to  $4^{\circ}$  and  $\Theta \pm 2^{\circ}$  for  $\Theta = 10^{\circ}, 20^{\circ}, \dots, 70^{\circ}$ .

**Figure 3.** The experimental spectrum.

The experimental data derived from the experimental spectrum are shown in Table 4. The experimentally measured total intensity of muons is  $I_0 = 49.64 \frac{c}{s}$ . It is based on the total count and the total time of measurement. Then, we use the counts from Table 4 for a given angle interval and determine the experimental  $I_0$ . This number, however, is not due only to the muons of the same incident angle. However, by using the formula  $I_{\Theta} = I_0 \cos^{1.85}(\Theta)$  [3] we can estimate the count rate of muons with that given incident angle. If we want to determine the influence of muons of the other incident angles, we simply calculate the ratio of the experimental  $I_0$  and this calculated value.

**Table 4.** The experimental data.

	Angle interval							
	$0^\circ-4^\circ$	$8^\circ-12^\circ$	$18^\circ-22^\circ$	$28^\circ-32^\circ$	$38^\circ-42^\circ$	$48^\circ-52^\circ$	$58^\circ-62^\circ$	$68^\circ-72^\circ$
Number of canal	7	12	28	50	80	129	233	555
Initial energy [MeV]	9.16	9.18	9.64	10.34	11.62	13.85	17.83	25.68
Final energy [MeV]	9.23	9.30	9.92	10.82	12.42	15.13	20.15	31.20
Count [ $\times 100$ ]	53914	54822	58966	57494	44823	26517	10944	2644

The results, which are normalized on the peak intensity and on the effective areas of the detector are shown in Table 5.

**Table 5.** Experimental results.

Angle interval $\Theta$ [ $^\circ$ ]	Rate from $\Theta$ [%]	Rate from other angles [%]
$0^\circ-4^\circ$	98	2
$8^\circ-12^\circ$	91	9
$18^\circ-22^\circ$	73	27
$28^\circ-32^\circ$	58	42
$38^\circ-42^\circ$	50	50
$48^\circ-52^\circ$	50	50
$58^\circ-62^\circ$	56	44
$68^\circ-72^\circ$	69	31

#### 4. Conclusions

The simulated results confirmed our assumption that the deposited energy of muons that are generated at the same incident angle is a very weak function of the energy of muons. The deposited energy is a very strong function of the initial angle of muons. For this function in this paper we made a fit with  $r^2 = 0.999875$ .

We showed that the shapes of the spectra of muons that are generated wby the different energies and different initial angles are the same.

Comparing the results of the simulation and of the experiment by looking at Tables 3 and 5 we can observe big differences for the beams with incident angles of  $\Theta = 10^\circ, 20^\circ$  and  $30^\circ$ . We can explain this by the fact that the peaks of the deposited energy for these angles are very close and because of that the spectra are interleaved. Thus we were not able to precisely determine the rate of the muons for these incident angles. On other hand, for  $\Theta = 40^\circ, 50^\circ, 60^\circ$  and  $70^\circ$  the estimated rates of muons for simulated and experimental results are consistent.

The difference between the simulated results and the experimental ones can be explained by the fact that in our simulation we did not include all real effects that appeared in the experiment. For example, we did not include the scintillation mechanism (we just calculated the deposited energy), and the muon beams were generated in very rough steps of energy and angle.

## References

1. S. Agostinelli et al., "*Geant4 - a simulation toolkit*", Nuclear Instruments and Methods in Physics A **506**, (2003).
2. <http://geant4.web.cern.ch/geant4/>
3. P. K. F. Grieder, "*Cosmic Rays at Earth*", Elsevier, Amsterdam, (2001).

## Determination of Backscatter Effects Variation for Different Shield Materials in Low Energy Gamma Spectrometry Using Geant4 Simulation Toolkit

N. Jovančević, M. Dorocki, G. Šoti, D. Mrdja, N. Todorović, J. Slivka, M. Vesković,  
M. Krmar, S. Forkapić, J. Papuga

*Department of Physics, Faculty of Sciences, University of Novi Sad,  
Trg Dositeja Obradovića 4, 21000 Novi Sad, Serbia*

Received: November 20, 2008

### Abstract

In order to decrease backscatter effect in low energy gamma spectrometry, there is the need to find the relationship between the backscatter peak and the free air volume. We expected that surface under backscatter peak to decrease with the increase in volume, but we could not make the volume too large because of rising of the concentration of  $^{222}\text{Rn}$ . The goal was to find optimal value of the free air volume for two types of shield, one made of Fe and the other of Pb. The experiment was simulated in Geant4 simulation toolkit, for 16 different geometries and for both shield types.

*Key words:* Backscatter peak, geometry of Pb and Fe shield, Geant4 simulation toolkit

## 1. Introduction

### 1.1. Photon Interaction with Matter

There are three main interactions of x-rays and  $\gamma$ -rays in matter: Photoelectric Effect, Compton Scattering and Pair Production.

The photoelectric effect involves the absorption of a photon by an atomic electron with the subsequent ejection of the electron from the atom. The ejected electron will slow down in the surrounding material and its energy will be absorbed. After the electron leaves the atom, we have a hole instead in the electron shell, and the atom will deexcitate with one or more x-rays or Augers electrons. Because of this, in most cases of photoelectric effect all energy of ingoing photon is absorbed in material. Result of this effect is the appearance of full energy peak in the gamma spectrum (Fig. 1). Another consequence is K and L x-ray peaks in low energy gamma spectrum, also seen in Fig. 1.

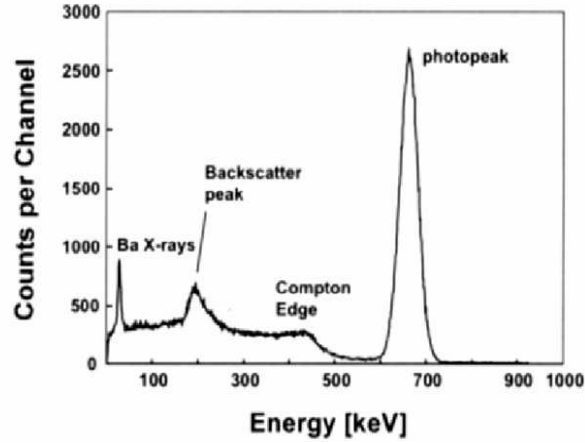


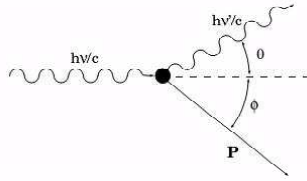
**Figure 1.** Typical pulse height spectrum of radiation emitted generated by a  $^{137}\text{Cs}$  source detected in a NaI(Tl) scintillation crystal.

The process of pair production involves the transformation of a photon into an electron-positron pair. In order to conserve momentum, this can only occur in the presence of a third body, usually a nucleus. Moreover, to create the pair, the photon must have at least energy of  $1.022\text{MeV}$ . Consequences of pair production are single and double escape peak, because of one or two gamma rays can escape from the detector crystal.

## 1.2. Compton Scattering

In the Compton Scattering process, only one part of photon energy is delivered to the electron. While the scattered photon is changing its direction for a certain angle  $\theta$ , electron is moved by the angle  $\phi$ . Figure 2 illustrates this scattering process.

Applying energy and momentum conservation, the following relations can be obtained.



$$E' = \frac{E}{1 + \varepsilon(1 - \cos\theta)}$$

$$E_e = E \left[ 1 - \frac{1}{1 + \varepsilon(1 - \cos\theta)} \right]$$

$$\text{tg}\phi = \frac{1}{1 + \varepsilon \text{tg}\frac{\theta}{2}},$$

**Figure 2.** Kinematics of Compton scattering.

$$\text{where } \varepsilon = \frac{h\nu}{m_e c^2}.$$

For a very small angle  $\theta$ , the energy of scatter photon is almost the same as of the incoming gamma photon. However, for a bigger  $\theta$  the energy of scatter photon becomes smaller, but even for  $\theta = 180^\circ$  the scatter photon still have imposing energy. For example, for  $E = 1\text{MeV}$  it will be  $E' = 204\text{keV}$ . In this work, this is the case that is in our focus and it is called the backscatter effect.

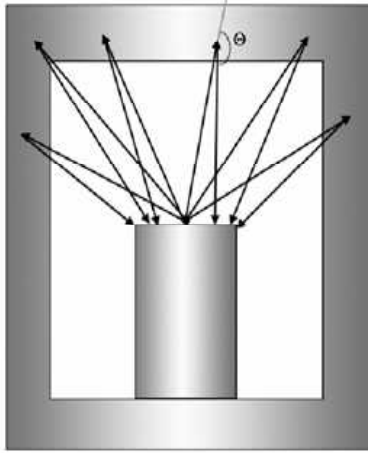


Figure 3. Backscatter effect.

## 2. Description of Simulated Experiment

We simulated gamma spectrum of radioactive point-like source  $^{60}\text{Co}$  which emitted gamma quanta with the energies of  $1332.5\text{ keV}$  and  $1173.2\text{ keV}$ .

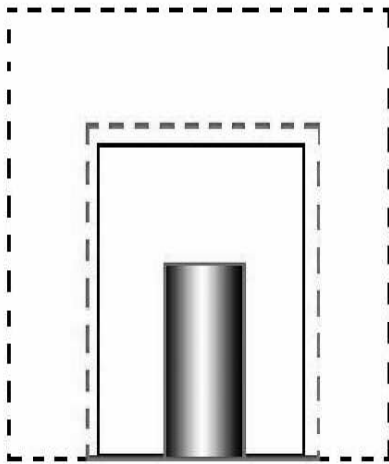


Figure 4. Scheme of changing the shield size.

In Figure 3 we can see the scheme of our system of the detector and shield, with tracks of gamma rays before and after the Compton scatter at a very big angle. This effect yields peak in low energies in the gamma spectrum (Figure 1).

Detection was made by simulation of HPGe GMX detector, with relative efficiency of 32 % inside of  $\text{Pb}$  shield. The simulated detector is the same as the real detector that has the Nuclear Laboratory, Department of Physics, University of Novi Sad. The idea was to find what happens with the backscatter region if we change the size of shield and its material.

In Figure 4 we can see the scheme of changing the shield size. The red color shows the case when the shield is proximate to the detector, and the black the case when the shield is uttermost from the detector.

Experiment was simulated in simulation toolkit Geant4 and the results were presented using software Mathematica and TableCurve2D.

## 3. Results and Discussion

We simulated 16 spectra with the statistics of  $2 \cdot 10^6$  events from the source  $^{60}\text{Co}$  for  $\text{Fe}$  shield and another 16 spectra using  $\text{Pb}$  shield. Figure 5 shows the spectrum of gamma radiation of  $^{60}\text{Co}$  source in the case when the  $\text{Fe}$  shield is close to the detector. In that case we have a maximum of the backscatter effect and we can see it in the region from  $100\text{ keV}$  up to  $300\text{ keV}$ . There are some more peaks that we found on this spectrum. At  $821\text{ keV}$ , there is a single gamma escape peak, then at  $310\text{ keV}$  we have a double escape peak, which

are results of pair production from the gamma quant with the energy  $E_\gamma = 1332 \text{ keV}$ . We have two peaks of total absorption, and also two Compton edges at  $1118 \text{ keV}$  and  $963.4 \text{ keV}$ .

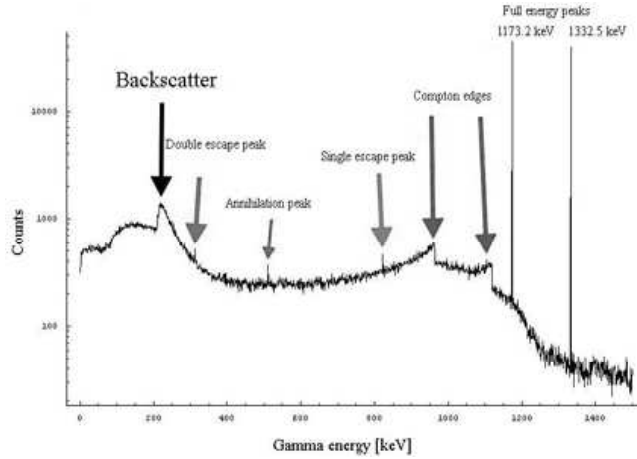


**Figure 5.** Spectrum of  $^{60}\text{Co}$  using  $\text{Fe}$  shield.

When we change the dimension of the shield, the backscatter region changes too. In the case of the  $\text{Fe}$  shield the difference between two positions for lower and highest backscatter peaks is shown in Figure 6. When the backscatter is lower, the shield position is uttermost, and for the highest backscatter peak, the shield is proximate.

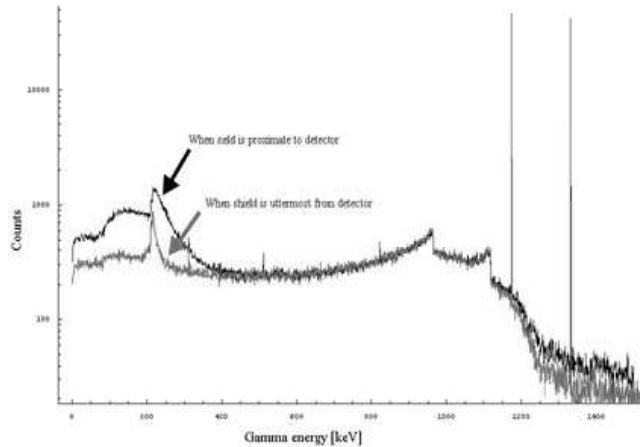


**Figure 6.** Spectrum for the cases when  $\text{Fe}$  shield is uttermost and proximate to detector.

If we put more spectra on one graph then we can see that in the beginning the backscatter region collapses fast with increasing the shield volume, and later it collapses slower (Fig. 7).

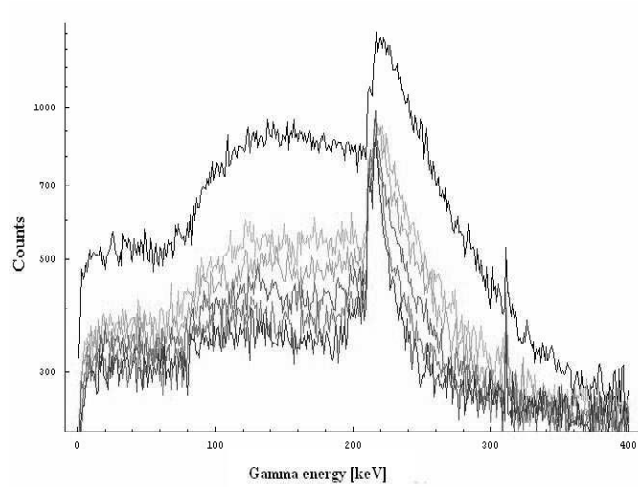


**Figure 7.** Reduction of the backscatter region for *Fe* shield.

However, using *Pb* shield this change is much smaller. We can see this in Figure 8.

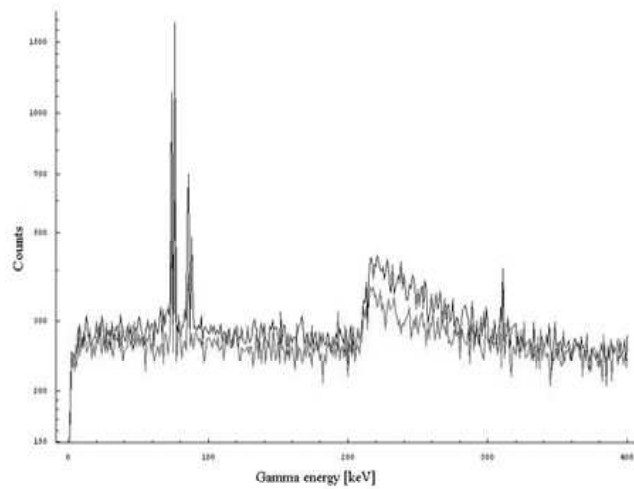


**Figure 8.** Reduction of backscatter peak for extreme geometries of *Pb* shield.

The surface under each backscatter region and continuum was a sum as presented in Tables 1 and 2. In the extreme case when the *Fe* shield is close to the detector ( $y \approx 0\text{ mm}$ ,  $r = 40\text{ mm}$ ), the sum in the backscatter region is equal 174,200 events, and the sum in the continuum to the first total absorption peak is 479,400 events.

In the extreme case when the *Fe* shield is close to the detector ( $y \approx 0\text{ mm}$ ,  $r = 40\text{ mm}$ ), the sum in the backscatter region is equal 74,500 events, and the sum in the continuum to the first total absorption peak is 363,400 events.

**Table 1.** Surfaces under continuum and backscatter peak for *Fe* shield.

$y$ [mm]	30		60		90	
$IR$ [mm]	Continuum counts	Backscatter counts	Continuum counts	Backscatter counts	Continuum counts	Backscatter counts
45	472300	113300	390200	108200	389000	107000
55	384200	104000	376500	98000	375600	96600
70	371000	94000	362900	87400	360000	85700
90	361100	86100	351100	78200	348000	76200
110	355100	82100	345700	73300	340700	70400

**Table 2.** Surfaces under continuum and backscatter peak for *Pb* shield.

$y$ [mm]	30		60		90	
$IR$ [mm]	Continuum counts	Backscatter counts	Continuum counts	Backscatter counts	Continuum counts	Backscatter counts
45	334400	60400	332200	59900	332000	59800
55	331500	59300	329300	58000	329000	58200
70	328900	58100	326500	57000	326000	56700
90	326800	56900	324700	56000	324000	55500
110	325700	56500	322400	55000	323900	55200

We calculated the free air volume between the shield and the detector and fitted the function of backscatter counts of that volume. The fitting was done by software TableCurve2D, and the function has the form:

$$y = a + bx + cx^{0.5} + \frac{d}{x^2} + ee^{-x},$$

where the coefficients values are given in Table 3 and graphs in Figures 9 and 10.

**Table 3.** Values of coefficients.

Coefficient	Value for <i>Fe</i> shield	Value for <i>Pb</i> shield
$a$	105123.05	62901.508
$b$	-1.4457492	0.61288346
$c$	-216.30794	-138.00144
$d$	$4.0545041 \cdot 10^9$	32334846
$e$	$-2.4059346 \cdot 10^{10}$	$-1.9018995 \cdot 10^8$

This drift of backscatter counts behaviour signify that we should increase *Fe* shield interior more than  $10 \text{ dm}^3$  in order to put backscatter effect on acceptable level.

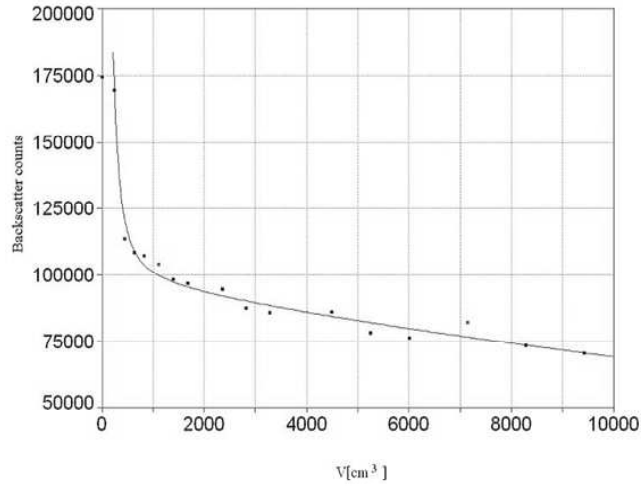


**Figure 9.** Backscatter counts dependence on the inner air volume for *Fe* shield.

When using the *Pb* shield we have a different situation. After a volume of  $8 \text{ dm}^3$  the backscatter peak reduction is slow.

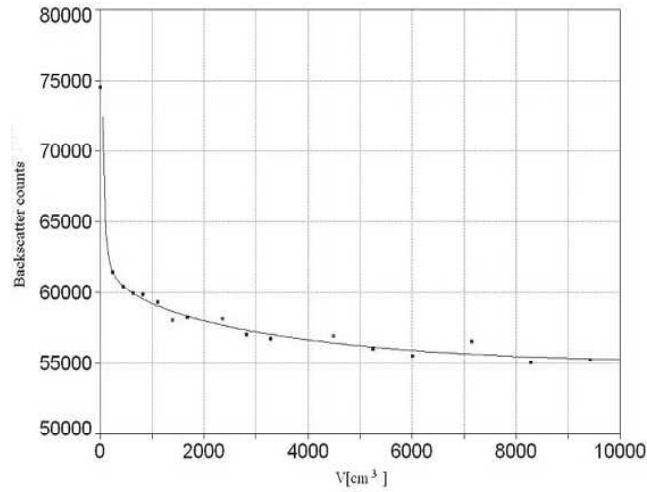


**Figure 10.** Backscatter counts depending on inner air volume for *Pb* shield.

#### 4. Conclusion

Keeping in mind the significant influence of the backscatter effect on the low energy region of a gamma spectrum and thus on the minimal detectable activity we simulated the HPGe detector spectra using point  $^{60}\text{Co}$  source placed directly in front of the detector. The useful volume enclosed by the shield can not be increased infinitely because the amount of radon is increasing as well. If the inner volume is too big, one cant eliminate the radon efficiently, allowing radon to induce the large portion of the background events.

Simulation results have shown that the backscatter effects appear in the region from  $100 \text{ keV}$  to  $300 \text{ keV}$  with a maximum at  $220 \text{ keV}$ . In this region, the count rates are

2.3 times higher for *Fe* shield that is proximate to the HPGe detector than for the *Pb* shield in the same position. It has been shown that by increasing the shield size from the smallest to the biggest, the backscatter region is reduced by 60 % (for *Fe* shield) and by 25 % (for *Pb* shield).

The relation found between the backscatter counts and shield free inner volume shows that in both cases (*Fe* and *Pb* shield) with the initial increase in the free inner volume the backscatter effect is rapidly decreasing to a volume of  $1.5 \text{ dm}^3$  (reduction by 44 % for *Fe* and 22 % for *Pb* shield). The further increase of the volume from  $1.5 \text{ dm}^3$  to  $10 \text{ dm}^3$  leads to the backscatter effect reduction by 30 % for *Fe* shield and 5 % for *Pb* shield.

The simulations results show that *Pb* shield is more convenient than *Fe* shield in respect of reducing the backscatter counts. Moreover, it has been estimated that *Pb* shield free inner volume should be around  $8 \text{ dm}^3$ . Knowing that the backscatter effect is properly reduced it is possible to use samples with bigger volume, and radon can be finely “irrigated” with gaseous nitrogen from a Dewar’s tank containing liquid nitrogen that is used to cool down the detector. In case of the *Fe* shield, the solution is in using shield with free inner volume of  $15 \text{ dm}^3$ . In all considerations we recommend that the distance between the detector front and shield interior should be about the same as the distance between lateral detector surface and shield interior.

## References

1. J. Slivka, I. Bikit, M. Vesković, Lj. Čonkić, , *Gamma Spectrometry - Special Methods and Applications*, Univerzitet u Novom Sadu, Novi Sad (2000) (in Serbian).
2. W.R. Leo, *Techniques for Nuclear and Particle Physics Experiments* (Springer-Verlag, Germany, 1994).
3. Geant4 Collaboration, Geant4 - a simulation toolkit (2003).  
<http://geant4.web.cern.ch/geant4/>
4. CERN Program Library Long Writeup W5013, Geant Detector Description and Simulation Tool (CERN Geneva, Switzerland, 1994).
5. Physics Reference Manual, Version: Geant4 9.1 (14 December, 2007).
6. Geant4 Collaboration, Geant4 User’s Guide for Application Developers (December 2007).

## Asymmetry of the Central Part of $H_\beta$ Spectral Line

S. Djurović, M. Ćirišan

Faculty of Sciences, Department of Physics, Trg Dositeja Obradovica 4, 21000 Novi Sad,  
Serbia

Received: *September 28, 2008*

### Abstract

Asymmetry of the central part of  $H_\beta$  spectral line has been experimentally studied and the results are presented in this paper. Relation between the blue and the red peaks of  $H_\beta$  line has been analyzed. All data, obtained in this work, have been compared with available theoretical and other experimental data.

*Key words:* Spectral line, line asymmetry

### 1. Introduction

The knowledge on theoretical and experimental profiles of hydrogen Balmer  $H_\beta$  line is very important for plasma diagnostics purposes. Determination of electron density from the Stark broadened profile of Balmer beta line is a standard technique in plasma spectroscopy.

Many experiments and theoretical calculations were focused on the analysis of this profile. Comprehensive analysis of experimental and theoretical works on  $H_\beta$  line asymmetry is given in Ref 1. Here, only short overview will be given. Some authors analyse in particular the central structure of  $H_\beta$  line [2 - 12], the dependence of  $H_\beta$  dip on the emitter-perturber-ion reduced mass [13 - 19], measured peak shifts or central dip shifts [20 - 22].

It is well known that there are two peaks, blue and red, in the central part of  $H_\beta$  line emitted from plasmas [5 - 12]. Many theoretical calculations, as well as the most commonly used theories - Griem [23] and Vidal et al. [24], give symmetrical and unshifted hydrogen line profiles.

Experimentally determined asymmetry has been explained by Kudrin and Sholin [25]. This theory takes into account the ion-atom quadrupole interaction, but the ratio of the two maxima given by this theory is too high. There are a few more recent theories which allow us to analyse the  $H_\beta$  line peaks asymmetry: Demura et al [26, 27], Halenka [8], Gigosos and Gonzalez [28] and Gunter and Konies [29].

Here, we have analysed the peaks' asymmetry i.e. relation between the blue and the red maximum of  $H_\beta$  line. Furthermore, we have compared our experimental results with

other experimental results [5, 7, 10-12], as well as with earlier and more recent theoretical results [25-28].

The main aim of this paper was to check theoretical calculations giving asymmetrical  $H_\beta$  line profiles [26-28], which were not included in this kind of analysis in the literature up to now. Therefore, we conducted two experiments. One was performed on T-tube plasma with electron densities  $(1 - 9) \cdot 10^{23} m^{-3}$  and electron temperatures  $17000 - 45000 K$ . Second experiment was performed on wall stabilized electric arc with electron densities  $(1.6 - 3.6) \cdot 10^{22} m^{-3}$  and electron temperatures between  $10000 K$  and  $11000 K$ .

Comparison of our results with the results from other experiments has been presented in this paper, as well.

## 2. Experimental Setup

In the first experiment, an electromagnetically driven T-tube, having a diameter of  $27 mm$  and being supplied with a reflector, has been used as a plasma source. The T-tube was energized using a  $4 \mu F$  capacitor bank, charged up to  $20 kV$ . The filling gas was hydrogen at a pressure of  $300 Pa$ . Spectroscopic observations of plasma were performed using a  $1 m$  monochromator and a photomultiplier. The observation point was fixed at  $4 mm$  in front of the reflector. Photomultiplier signals were recorded by an oscilloscope.  $H_\beta$  profiles were scanned at close intervals using successive discharges over the wavelength range  $\pm 30 nm$  from the line center. More details on this experiment can be found in Ref. 1.

In the second experiment, plasma source was a wall stabilized electric arc operating in argon at the atmospheric pressure. About 2% of hydrogen was being introduced in the central part of the arc. The current of about  $30 A$ , was supplied to the arc by a current-stabilized power supply. Experimental details on this experiment can be found in Refs. 30 and 31.

## 2. Plasma Diagnostics

Electron densities of the T-tube plasma, ranging from  $9.6 \cdot 10^{22} m^{-3}$  to  $8.9 \cdot 10^{23} m^{-3}$ , were determined from Stark widths of the H $\beta$  line profiles. These measurements were performed in conjunction with theoretical calculations by Griem [23]. The estimated uncertainties of the electron densities do not exceed  $\pm 9\%$ . Electron temperatures, ranging from  $17000 K$  to  $45000 K$ , were determined from line - to - line continuum ratios for  $H_\beta$  line [32]. The uncertainties for electron temperature measurements were between  $\pm 8\%$  and  $\pm 15\%$ , from the lower to the higher values respectively.

Electron densities of wall stabilized arc plasma, ranging from  $1.6 \cdot 10^{22} m^{-3}$  to  $3.6 \cdot 10^{22} m^{-3}$ , were determined from measured Stark widths of the  $H_\beta$  line [24]; while electron temperatures, ranging from  $10000 K$  to  $11000 K$ , were determined using Saha equation [33].

## 2. $H_\beta$ Profile Recording and Data Processing

In general, the intensity measurements of radiation from pulsed sources, such as electromagnetically driven shock T-tube, give scattered points due to a very short observation time and certain plasma irreproducibility. This makes a detailed analysis of the  $H_\beta$  line

profile rather difficult, especially the part of the profile maxima. The influence of the points scattering was minimized by obtaining each point of the recorded profile as an average value of six measurements.

Signal intensities have been normalized to the spectral sensitivity of the optical system. This must be necessarily done, since the experimental profiles of  $H_\beta$  line are rather broad - several tens of nanometers.

Before measuring the blue and the red peak intensities, continuum level has been determined and subtracted. The continuum level was determined using an asymptotic formula  $I = f(\Delta\lambda^{-5/2})$  [32], which describes the behaviour of the intensity at the line wings. Details on data processing can be found in Ref. 1, where possibilities of selfabsorption were discussed as well.

Examples of recorded  $H_\beta$  line profiles from both experiments are presented in Fig. 1a and 1b. The points in Fig. 1a correspond to averaged oscilloscope intensities; while  $H_\beta$  line intensities in Fig.1b were obtained using a strip-chart recorder.

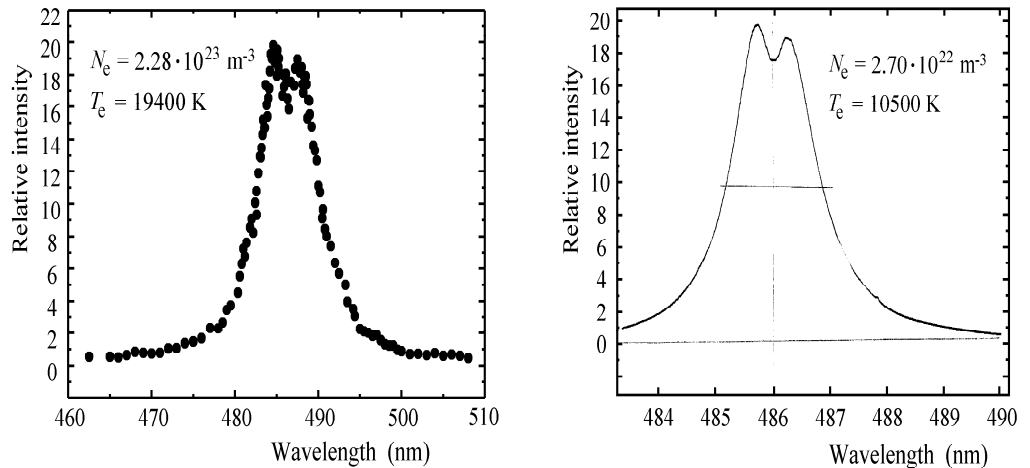


**Figure 1.**  $H_\beta$  line profile examples. a) T-tube experiment, b) stabilized arc experiment.

#### 4. Results and Discussion

In this study, the intensities of  $H_\beta$  line peaks have been measured and their relation has been analyzed. Definition of the measured  $H_\beta$  line asymmetry parameter is shown in Fig. 2.

The  $H_\beta$  line asymmetry parameter represents the relative difference between the maximal intensity of the blue peak  $I_B$  and the red peak  $I_R$  of  $H_\beta$  line:

$$\delta I = \frac{I_B - I_R}{I_B} \quad (1)$$

A comparison between different theoretical data [1, 25, 28], our experimental data and experimental data from other authors [10 - 12], for a wide range of electron density, is shown in Fig. 3. The experimental errors are in the range  $\pm(14\% - 19\%)$  for T-tube experiment and  $\pm(16\% - 20\%)$  for pulsed arc experiment. The results given for pulsed arc experiment [34] correspond to electron densities  $(1.5 - 7) \cdot 10^{22} m^{-3}$  and electron

temperatures of about 104 K. More details on pulsed arc experiment can be found in Ref. 9. In addition, present results are compared with experimental results from [10 - 12]. In Fig. 3, only experimental results obtained from pure hydrogen plasmas are presented.

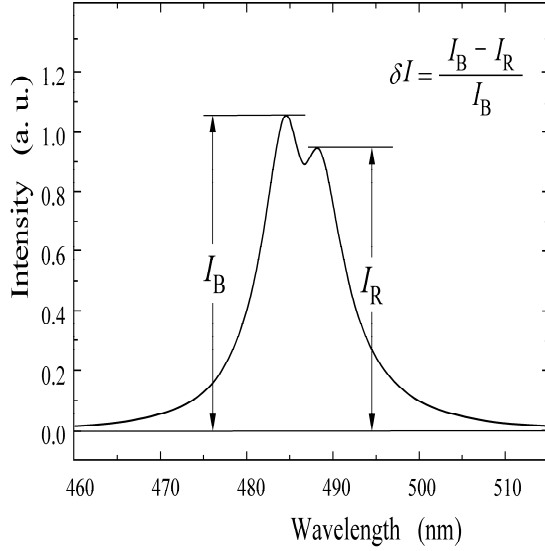


**Figure 2.** Illustration of measured  $H_\beta$  line asymmetry parameter.

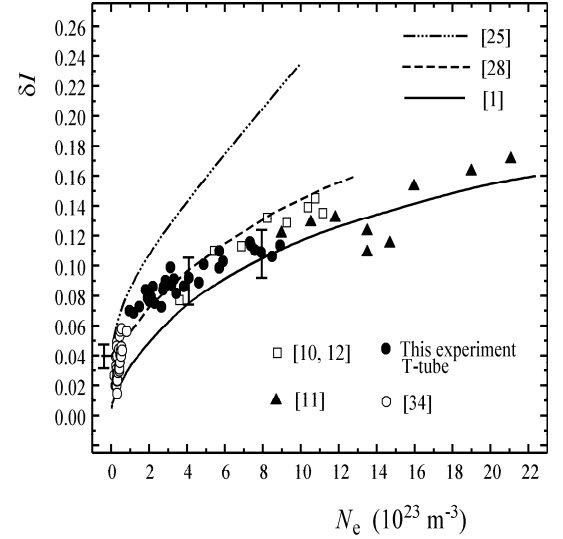


**Figure 3.** Relative difference between the two  $H_\beta$  peaks' intensities as a function of electron density. Experiments and theories correspond to pure hydrogen plasmas.

All experimental results, obtained from four different experiments, show good agreement and a certain general trend, i.e. the values of  $H_\beta$  line asymmetry parameter increase for higher electron densities. There is, obviously, a disagreement between measured and calculated data from [25]. Theoretical curves presented by a full and a dashed line in Fig. 3, have been obtained from recently calculated  $H_\beta$  profiles [1, 28]. These theoretical results much better describe the trend of experimental points. The agreement of experimental points and theoretical results from [1] is a little bit better for higher electron densities; while the agreement of experimental data and theoretical results from [28] is a little bit better for lower electron densities. In general, both theoretical results follow the experimental points trend.

Using standard numerical analysis method we found the best fit for experimental and theoretical results using simple function:

$$\delta I = a \times N_e^b \quad (2)$$

where  $N_e(10^{23} m^{-3})$  is the electron density. The fitting results are given in Table 1.

**Table 1.** The coefficients  $a$  and  $b$  of the function given by equation (2 ).

Source	$a$	$b$
Theory [1]	0.0375	0.4746
Theory [25]	0.1037	0.3546
Theory [28]	0.0610	0.4860
Experiments, present and [10 - 12]	0.0615	0.3301

Standard deviation between the measured points and the best fit of equation (2 ) was less than 9.55.

Results of the measurement of the relative difference between the maxima of the two  $H_\beta$  peaks, obtained from wall stabilized arc experiment with 98%  $Ar + 2\% H$  plasma, are presented in Fig. 4. In this figure, results from [5, 7] are compared with our results. Experimental errors in wall stabilized arc experiment were about  $\pm 12\%$ .

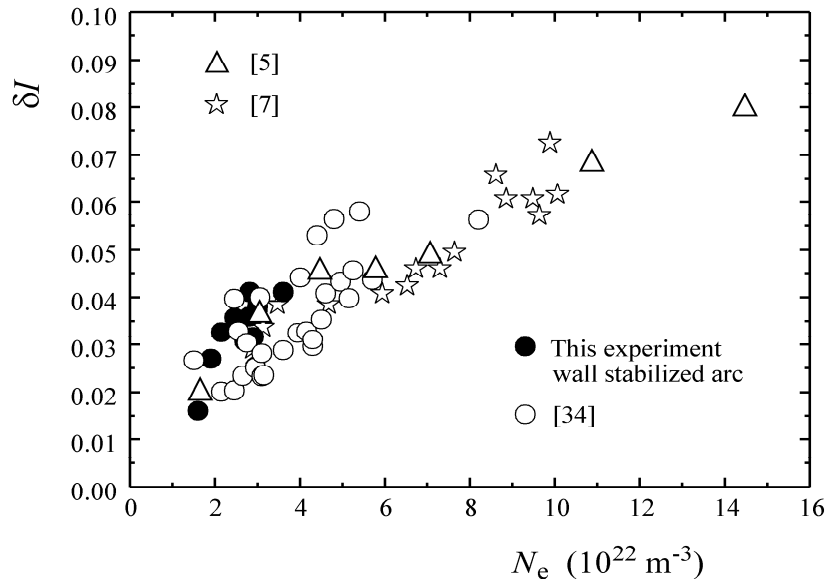


**Figure 4.** Relative difference between the two  $H_\beta$  peaks' intensities as a function of electron density. Experiments correspond to argon-hydrogen plasmas, except the pulsed arc experiment.

These results are separated from the results in Fig. 3 because of two reasons. First, the structure of the data for lower electron densities would not be visible because of the big range in electron density scale. Second, it is well known that ion dynamic effect has influence on the structure of the central part of  $H_\beta$  line and this influence depends on the reduced mass value [14 - 19]. In order to compare the results from pure hydrogen plasmas and argon-hydrogen plasmas, results from pulsed arc experiment have been included in

Fig. 4, in addition. All data are in good agreement and there is no distinction between these two groups of data.

The results from Fig. 4 show that ion motion effect has no or at least no significant influence on relation between the blue and the red maximum. It influences only the minimal intensity of the  $H_\beta$  line central part. This is in agreement with experiment [15]. In [15], experimental  $H_\beta$  profiles corresponding to both pure hydrogen and mixed argon-hydrogen plasma conditions were compared. The authors analyzed the relative dip:

$$D_I = \frac{I_{max} - I_{min}}{I_{max}}$$

where  $I_{max} = \frac{I_B + I_R}{2}$ , and  $I_{min}$  is dip intensity.

In the present paper, as asymmetry parameter of the central part of  $H_\beta$  line we have been analyzing the relative difference between the  $H_\beta$  line peaks' intensities  $\delta I$ . We used this parameter in order to be able to make comparisons with other experimental results [5, 7, 10 - 12]. However, the parameter which is usually used for describing the spectral line asymmetry is:

$$A_{BR} = \frac{I_B - I_R}{I_B + I_R}$$

(see Ref. 1 and references therein). So, we propose the use of this parameter instead of the relative difference of peaks' intensities  $\delta I$  for these types of analyses in the future. The dependence of  $\delta I$  and  $A_{BR}$  on electron density have the same trend, which is illustrated in Fig. 5. For this illustration we used only our T-tube experimental data.

In T-tube experiment selfabsorption was less than 2% [1]. Besides the selfabsorption, the emission from the cold layer, formed near the tube wall, can also occur.  $H_\beta$  profiles emitted from cold layers are substantially narrower than the profiles emitted from the hot plasma. The presence of the emission from cold layers could influence the central part of observed profile, as well as the discussed asymmetry parameters, especially the relative dip. The thickness of cold layer is changing during the plasma life, but it was much smaller than 1 mm during the plasma observation [1]. The emissivity from the cold layer is considered to be much smaller than radiation from hot plasma due to its much smaller radiation volume. Thus, for this experimental conditions the influence of the cold layer could be discarded.

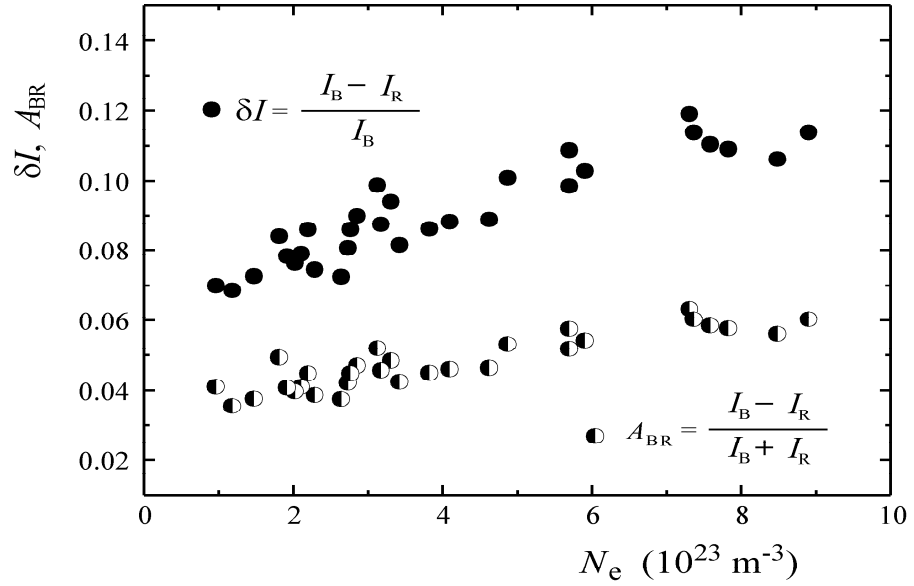


**Figure 5.** Relative difference of  $H_\beta$  peaks' intensities and asymmetry parameter as a function of electron density.

#### 4. Conclusions

The subject of this study was asymmetry of the central part of the  $H_\beta$  line profile. The results of two plasma experiments and other experimental data allowed us to analyse the asymmetry parameters in a wide range of electron densities. The obtained results were compared with theoretical data [25] and especially with more recent theoretical data [1, 28].

This paper represents a part of investigations on the asymmetry of  $H_\beta$  spectral line profile. Its purpose, besides the comparison of the relative difference between  $H_\beta$  peaks' intensities  $I_B$  and  $I_R$  ( $\delta I$ ) with other experimental results [5, 7, 10 - 12, 34], is to check new theoretical results [1, 28]. There is a big disagreement between the old [25] and the new theoretical data [1, 28] (see Fig. 3).

Theoretical results from [1] fit to experimental points a little bit better for higher electron densities; while the agreement of experimental and theoretical results from [28] is a little bit better for lower electron densities. Both of these theoretical results follow the trend of experimental points.

These results can be useful in future analyses of the  $H_\beta$  line profile for plasma diagnostic purposes.

## Acknowledgments

This work is supported by Ministry of Science and Environmental Protection, Republic of Serbia under project 141024.

## References

1. S. Djurović, D. Nikolić, I. Savić, S. Sörge and A. V. Demura, *Phys. Rev. E* **71**, 036407 (2005).
2. D. D. Burgess and R. Mahon, *J. Phys. B: Atom. Molec. Phys.* **5**, 1756 (1972).
3. J. D. Hey and H. R. Griem, *Phys. Rev. A* **12**, 169 (1975).
4. H. Erich and D. Kelleher, *Phys. Rev. A* **21**, 319 (1980).
5. V. Helbig and K. P. Nick, *J. Phys. B* **14**, 3573 (1981).
6. Z. Mijatović, M. Pavlov and S. Djurović, *J. Quant. Spectrosc. Radiat. Transfer* **38**, 209 (1987).
7. J. Halenka, *J. Quant. Spectrosc. Radiat. Transfer* **39**, 347 (1988).
8. J. Halenka, *Z. Phys. D Atoms molecules and Clusters* **16**, 1 (1990).
9. F. Torres, M. A. Gigosos and S. Mar, *J. Quant. Spectrosc. Radiat. Transfer* **31**, 265 (1984).
10. C. Carlhoff, E. Krametz, J. H. Schäfer and J. Uhlenbusch, *J. Phys. B: At. Mol. Phys.* **19**, 2629 (1986).
11. J. Uhlenbusch and W. Viöl, *Contrib. Plasma Phys.* **29**, 459 (1989).
12. J. Uhlenbusch and W. Viöl, *J. Quant. Spectrosc. Radiat. Transfer* **44**, 47 (1990).
13. J. Seidel, *Z. Naturforsch. A* **32**, 1207 (1977).
14. D. E. Kelleher and W. L. Wiese, *Phys. Rev. Lett.* **31**, 1431 (1973).
15. W. L. Wiese, D. E. Kelleher and V. Helbig, *Phys. Rev. A* **11**, 1854 (1975).
16. R. W. Lee, *J. Phys. B: Atom. Molec. Phys.* **12**, 1145 (1979).
17. C. Fleurier, G. Coulaud and P. Ranson and J. Chapelle, *Phys. Rev. A* **121**, 851 (1980).

18. M. A. Gigosos and V. Cardenoso, *J. Phys. B: At. Mol. Phys.* **20**, 6005 (1987).
19. V. Cardenoso and M. A. Gigosos, *Phys. Rev. A* **39**, 5258 (1989).
20. J. Halenka and J. Musielok, *J. Quant. Spectrosc. Radiat. Transfer* **36**, 233 (1986).
21. S. Djurović, Z. Mijatović and R. Kobilarov, *Contrib. Plasma Phys.* **28**, 229 (1988).
22. J. Halenka, B. Vujičić and S. Djurović, *J. Quant. Spectrosc. Radiat. Transfer* **42**, 571 (1989).
23. H. R. Griem, *Spectral Line Broadening by Plasmas*, (Academic Press, New York, 1974).
24. C. R. Vidal, J. Cooper and E. W. Smith, *Astrophys. J. Suppl. Ser.* **25**, 37 (1973).
25. L. P. Kudrin and G. V. Sholin, *Soviet Physics-Doklady* **7**, 1015 (1963).
26. A. V. Demura and G. V. Sholin, *J. Quant. Spectrosc. Radiat. Transfer* **15**, 881 (1975).
27. A. V. Demura, V. V. Pleshakov and G. V. Sholin, Preprint No. IAE-5349/6, I. V. Kurchatov Institute of Atomic Energy, Moscow, p. 98 Atlas detaljnih Starkovskih konturov vodorodnih spektralnih linij v plotnoi plazme, (in russian) (1991).
28. M. A. Gigosos and M. Á. Gonzáles, B. Talin and A. Calisti, *17<sup>th</sup> International Conference on Spectral Line Shapes*, Paris (France), Frontier Group, ed. E. Dalimier, Paris 2004, p. 451, ISBN 2-914601-14-X (2004).
29. S. Gunter and A. Konies, *Phys. Rev. E* **55**, 907 (1997).
30. S. Djurović, Z. Mijatović, R. Kobilarov and N. Konjević, *J. Quant. Spectrosc. Radiat. Transfer* **57**, 695 (1997).
31. S. Djurović, D. Nikolić, Z. Mijatović, R. Kobilarov and N. Konjević, *Plasma Sources Sci. Technol.* **11**, 95 (2002).
32. H. R. Griem, *Plasma Spectroscopy*, (McGraw-Hill, New York, 1964).
33. C. H. Popenoe and J. B. Shumaker Jr., *J. Res. NBS, Phys. Chem A* **69**, 495 (1965).
34. M. A. Gigosos and M. Á. Gonzáles, private communication.

## Spin-wave Theory of Frustrated Magnetic Bilayers on Square Lattice

M. Pantić, D. Kapor, M. Pavkov-Hrvojević, M. Rutonjski, S. Radošević  
*Department of Physics, Faculty of Sciences, Novi Sad, Trg Dositeja Obradovića 4, Serbia*

Received: December 5, 2008

### Abstract

We investigate the magnetic properties of bilayers consisting of ferro- and anti-ferromagnetic layers within the framework of quantum spin  $S = 1/2$  Heisenberg model using the method of double-time temperature-dependent Green's functions (GF) within random-phase approximation (RPA) at finite temperature. Both ferro- and antiferromagnetic interlayer coupling is considered. The spin-wave excitation spectrum and four-sublattice magnetizations are calculated for both types of interlayer coupling. It is shown that in this system appear four branches of energy of elementary spin excitations. Numerical calculation indicate how the system properties depend on the magnitude and sign of interlayer exchange integrals. The presence of the frustration introduces interesting effects at low temperatures.

*Key words:* Spin-wave theory, ferro-antiferromagnetic bilayers, frustration, Green's function, random-phase approximation

### 1. Introduction

During the last several decades there has been a permanently increasing interest for the magnetic properties and excitations of low-dimensional magnetic materials, in particular, the attention being focused on the properties of layered magnetic systems, thin films and superlattices [1-9]. The magnetic properties of such artificial structures show many unique characteristics which are distinctly different from those of their bulk counterparts. A good understanding of the magnetic properties of these materials is important. The investigations of layered ferromagnets, antiferromagnets and ferrimagnets show that the interlayer coupling, though very small, is essential for a system realizing long-range order at nonzero temperature [10].

The investigations of superlattices and multilayers show that there are interesting effects in these systems composed either of two ferromagnetic materials or of alternating layers of ferro- and antiferromagnetic coupling at the interface and materials [11-14]. One should stress that the presence of an external field in such systems causes the appearance of numerous different phases and rather interesting transitions.

Quantum effects in bilayers consisting of ferro- and antiferromagnetic layers are analyzed using Green-function method within Tyablikov's approximation at low temperatures [15] with spin Hamiltonian. However, there recently appeared papers analyzing properties of bilayer structures in bosonic approximation [16, 17].

In this paper we analyze the bilayer, i.e. the system consisting of ferro- and antiferromagnetic layers on simple cubic structure where the layers are coupled either ferro- or antiferromagnetically. This structure is rather interesting for the theoretical analysis since in such systems there appears the frustration and also quantum fluctuations. This system consists of a plane ordered antiferromagnetically with sublattices denoted by  $a_1$ ,  $a_2$  and the ferromagnetic layer with corresponding sublattices  $b_1$ ,  $b_2$ . The spin structure of our bilayer is presented in the Figure 1. Intralayer exchange integrals are denoted by  $J_a$  and  $J_b$ , respectively. Interlayer coupling is either ferro- or antiferromagnetic. The system is under the action of external magnetic field directed along the  $z$ -axis and there also exists spin anisotropy of  $XXZ$  type. The presence of this anisotropy is necessary due to the fact that the system behaves like a quasi 2D system.

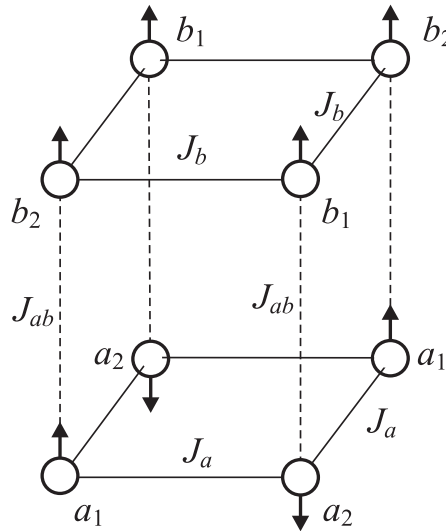


**Figure 1.** Schematic representation of spin structure of the bilayer system.

It is very well known that in 1D or 2D isotropic Heisenberg ferromagnets and antiferromagnets, no magnon energy gap appears in the excitation spectrum and there can not exist long-range magnetic order at finite temperatures (Mermin and Wagner theorem [18]). In reality, long-range order in quantum 2D magnetic systems exists and it can be caused by external magnetic field, single-ion anisotropies, exchange-interaction anisotropies, or magnetic dipole-dipole interaction, etc.

The previous theoretical studies [16, 17] solved this problem within the Heisenberg model in bosonic approximation. Similar system is also analyzed in the paper [15] within the spin formalism, although numerical analysis of the spin-wave excitation spectrum possesses one essential drawback. In that paper, namely, just as in the recently published works of the Chinese group, there appears the problem of negative energy branches as well as their non-physical and rather complex interpretation. Actually, the authors of those papers plot in the vicinity of absolute zero negative energy branches which is incorrect and

meaningless from the physical point of view. We have recently analyzed this problem in detail for the system of three-layer ferrimagnetic superlattice and the results were published in the papers [4] and [6].

In this paper, we present an analysis of a dispersion relation, analytic expressions for temperature dependence of the four-sublattice magnetization and corresponding expressions for quantum spin fluctuations at low temperatures. We have shown that in the system there exist four real energy branches, three of them positive and one negative. We have also shown, according to our papers [4, 5, 6], how to determine the remaining positive energy branch(es) which we have evaluated numerically, for a certain choice of system parameters and plotted in Figure 2.

The paper is organized as follows. In Section 2 we define the model and using the formalism of Green's function we determine the spectrum of elementary excitations using random-phase (RPA) or Tyablikov's decoupling of higher order GFs. Four-sublattice magnetizations were determined analytically in Section 3. The energy of elementary magnon excitations in systems for the canted spin configuration was also analyzed numerically in a self-consistent manner. The conclusions are reviewed in Section 4.

## 2. Hamiltonian of the System and Spin-wave Spectrum

Our theoretical analyses are based on the Heisenberg magnetic exchange model with nearest neighbor interaction within the magnetic layers. We consider a model consisting of two layers with a square lattice structure. The first layer is antiferromagnetically ordered while the second is ferromagnetic. In the presence of an external field (along the  $z$ -direction), the magnetic Hamiltonian is written as follows:

$$\begin{aligned}
\hat{H} = & \sum_{\vec{q}, \vec{\lambda}} \left[ \frac{1}{2} J_a \left( \hat{S}_{\vec{q}}^+(a_1) \hat{S}_{\vec{q}+\vec{\lambda}}^+(a_2) + h.c. \right) - (J_a + D_a) \hat{S}_{\vec{q}}^z(a_1) \hat{S}_{\vec{q}+\vec{\lambda}}^z(a_2) - \right. \\
& \left. - \frac{1}{2} J_b \left( \hat{S}_{\vec{q}}^+(b_1) \hat{S}_{\vec{q}+\vec{\lambda}}^-(b_2) + h.c. \right) - (J_b + D_b) \hat{S}_{\vec{q}}^z(b_1) \hat{S}_{\vec{q}+\vec{\lambda}}^z(b_2) \right] \\
& - \sum_{\vec{q}} \left[ \frac{1}{2} J_{ab} \left( \hat{S}_{\vec{q}}^+(a_1) \hat{S}_{\vec{q}}^-(b_2) + h.c. \right) + (J_{ab} + D_{ab}) \hat{S}_{\vec{q}}^z(a_1) \hat{S}_{\vec{q}}^z(b_2) - \right. \\
& \left. - \frac{1}{2} J_{ab} \left( \hat{S}_{\vec{q}}^+(a_2) \hat{S}_{\vec{q}}^+(b_1) + h.c. \right) - (J_{ab} + D_{ab}) \hat{S}_{\vec{q}}^z(a_2) \hat{S}_{\vec{q}}^z(b_1) \right] \\
& - g \mu_B \mathcal{H} \sum_{\vec{q}} \left[ \hat{S}_{\vec{q}}^z(a_1) - \hat{S}_{\vec{q}}^z(a_2) + \hat{S}_{\vec{q}}^z(b_1) + \hat{S}_{\vec{q}}^z(b_2) \right]
\end{aligned} \tag{1}$$

where  $J_a(D_a)$  and  $J_b(D_b)$  are intralayer antiferro- or ferromagnetic exchange (spin anisotropy) interactions in the first or second layer, respectively, and  $J_{ab}(D_{ab})$  are inter-layer (or spin anisotropy) interactions. These interactions are, irrespective of coupling type, taken to be the same, i.e. ferromagnetic or antiferromagnetic coupling. This way of taking into account the intralayer couplings leads to the frustration in such magnetic systems. The quantities  $g$  and  $\mu_B$  are Lande's  $g$ -factor and Bohr's magneton, respectively,  $\mathcal{H}$  is the  $z$ -component of the external field. Vector  $\vec{q}$  is the two-dimensional vector determining the position of the magnetic ions within the plane. In order to simplify the calculations, we performed the rotation of quantization axis in  $a_2$ -sublattice for  $180^\circ$ . Our primary aim is to determine the spectrum of the elementary excitations. The knowledge

of the spectrum will allow us to calculate the four-sublattice magnetizations and further on the transition temperature for the studied magnetic system. Let us note that in the particular magnetic system, due to present frustration, we have four-sublattice different magnetizations  $\langle \hat{S}_{\vec{\rho}}^z(a(b)_{1,2}) \rangle$ . For that purpose we shall use the spin GF method and introduce the following four-Green's functions:

$$G_{a_{1,2}}^{\pm}(\vec{\rho}, \vec{\rho}') = \langle \langle \hat{S}_{\vec{\rho}}^{\pm}(a_{1,2}) | \hat{B}_{\vec{\rho}'} \rangle \rangle, \quad G_{b_{1,2}}^+(\vec{\rho}, \vec{\rho}') = \langle \langle \hat{S}_{\vec{\rho}}^+(b_{1,2}) | \hat{B}_{\vec{\rho}'} \rangle \rangle, \quad (2)$$

and the corresponding system of GFs for the corresponding adjoint operators  $\hat{S}_{\vec{\rho}}^{\mp}(a_{1,2})$  and  $\hat{S}_{\vec{\rho}}^-(b_{1,2})$ , where  $\hat{B}_{\vec{\rho}'}$  is at present an arbitrary operator to be chosen in a suitable manner later. The higher order GFs appearing in the equations of motion for GF (2) will be decoupled first in the spirit of Tyablikov's approximation scheme [19]

$$\langle \langle \hat{S}_{\vec{\rho}}^z(a_{1,2}) \hat{S}_{\vec{\rho}}^{\pm}(a_{1,2}) | \hat{B}_{\vec{\rho}'} \rangle \rangle \longrightarrow \langle \hat{S}_{\vec{\rho}}^z(a_{1,2}) \rangle \langle \langle \hat{S}_{\vec{\rho}}^{\pm}(a_{1,2}) | \hat{B}_{\vec{\rho}'} \rangle \rangle, \quad \alpha_{1,2} = a_{1,2}(b_{1,2}) \quad (3)$$

A next step is the transition to inverse lattice by the following Fourier transformation:

$$\hat{S}_{\vec{\rho}}^{\pm} = \frac{1}{\sqrt{N_2}} \sum_{\vec{k}_{\parallel}} \hat{S}_{\vec{k}_{\parallel}}^{\pm} e^{i\vec{k}_{\parallel} \cdot \vec{\rho}} \quad (4)$$

where  $N_2$  is the number of unit cells within the layer. Thus, the system of equations for the Fourier components reads:

$$\begin{aligned} (E - \varepsilon_1) G_{a_1}^+(k_{\parallel}) + J_{a_1}(k_{\parallel}) G_{a_2}^-(k_{\parallel}) + 0 \cdot G_{b_1}^+(k_{\parallel}) + \sigma_{a_1} J_{ab} G_{b_2}^+(k_{\parallel}) &= \frac{i}{2\pi} \langle [\hat{S}_{a_1}^+, \hat{B}] \rangle \\ J_{a_2}(k_{\parallel}) G_{a_1}^+(k_{\parallel}) + (E + \varepsilon_2) G_{a_2}^-(k_{\parallel}) - \sigma_{a_2} J_{ab} G_{b_1}^+(k_{\parallel}) + 0 \cdot G_{b_2}^+(k_{\parallel}) &= \frac{i}{2\pi} \langle [\hat{S}_{a_2}^-, \hat{B}] \rangle \\ 0 \cdot G_{a_1}^+(k_{\parallel}) + \sigma_{b_1} J_{ab} G_{a_2}^-(k_{\parallel}) + (E - \varepsilon_3) G_{b_1}^+(k_{\parallel}) + J_{b_1}(k_{\parallel}) G_{b_2}^+(k_{\parallel}) &= \frac{i}{2\pi} \langle [\hat{S}_{b_1}^+, \hat{B}] \rangle \\ \sigma_{b_2} J_{ab} G_{a_1}^+(k_{\parallel}) + 0 \cdot G_{a_2}^-(k_{\parallel}) + J_{b_2}(k_{\parallel}) G_{b_1}^+(k_{\parallel}) + (E - \varepsilon_4) G_{b_2}^+(k_{\parallel}) &= \frac{i}{2\pi} \langle [\hat{S}_{b_2}^+, \hat{B}] \rangle \end{aligned} \quad (5)$$

where  $J_{a_{1,2}(b_{1,2})}(k_{\parallel}) = z \sigma_{a_{1,2}(b_{1,2})} J_{a_{1,2}(b_{1,2})} \gamma(k_{\parallel})$ ,  $\sigma_{a(b)_{1,2}} = \langle \hat{S}_{\vec{\rho}}^z(a(b)_{1,2}) \rangle$ ,  $z$  is the number of in-plane nearest neighbors,

$$\begin{aligned} \varepsilon_1 &= z \sigma_{a_2} (J_a + D_a) + \sigma_{b_2} (J_{ab} + D_{ab}) + g \mu_B \mathcal{H}, \\ \varepsilon_2 &= z \sigma_{a_1} (J_a + D_a) - \sigma_{b_1} (J_{ab} + D_{ab}) - g \mu_B \mathcal{H} \\ \varepsilon_3 &= z \sigma_{b_2} (J_b + D_b) - \sigma_{a_2} (J_{ab} + D_{ab}) + g \mu_B \mathcal{H}, \\ \varepsilon_4 &= z \sigma_{b_1} (J_b + D_b) + \sigma_{a_1} (J_{ab} + D_{ab}) + g \mu_B \mathcal{H} \end{aligned} \quad (6)$$

while  $\gamma(k_{\parallel})$  is a geometrical factor given by

$$\gamma(k_{\parallel}) = \frac{1}{z} \sum_{\vec{\lambda}} e^{i\vec{k}_{\parallel} \cdot \vec{\lambda}} = \frac{1}{2} (\cos ak_x + \cos ak_y), \quad z = 4 \quad (7)$$

Here  $\vec{\lambda}$  is the nearest-neighbor displacement within one of the layers, and  $a$  the dimension of the 2D magnetic unit cell. One can easily obtain the adjoint system of equations, so it will not be explicitly quoted. The determinant of the system of Eqs (5) determines the energies of the elementary excitations in the spin system and it is given as:

$$\Delta(E) = \begin{vmatrix} E - \varepsilon_1 & -J_{a_1}(\vec{k}_{\parallel}) & 0 & \sigma_{a_1} J_{ab} \\ J_{a_2}(\vec{k}_{\parallel}) & E + \varepsilon_2 & -\sigma_{a_2} J_{ab} & 0 \\ 0 & \sigma_{b_1} J_{ab} & E - \varepsilon_3 & J_{b_1}(\vec{k}_{\parallel}) \\ \sigma_{b_2} J_{ab} & 0 & J_{b_2}(\vec{k}_{\parallel}) & E - \varepsilon_4 \end{vmatrix} \quad (8)$$

The energies of the system of the four-sublattice model are obtained by solving

$$\Delta(E) = 0 \quad (9)$$

One can see that it is a fourth-order algebraic equation in  $E$  and it has four real roots  $E_i$  ( $i = 1, 2, 3, 4$ ) corresponding to four branches of the spin-wave spectrum in some system parameter range. Analytic solution of this equation in the particular case of the system with frustration, can not be given. For this reason, we have performed the numerical analysis of the above equations for some particular parameters of the model. Since the energies of elementary magnetic excitations are expressed in terms of the corresponding sublattice magnetizations, further analysis demands the analytical expressions for magnetizations. In this way we form a closed set of equations which will be solved numerically in a self-consistent manner. The next section is devoted to the derivation of the expressions for four-sublattice magnetizations which are used, together with (9) to study numerically the spectrum of elementary magnetic excitations in the system.

### 3. Spontaneous Sublattice Magnetizations and Numerical Analysis

Let us determine the necessary magnetizations entering the expression for the energy (9). Starting from the system of equations (5) we calculate the four-sublattice magnetizations (for  $\mathcal{H} = 0$ ) in terms of the temperature and determine the corresponding quantum fluctuations of the magnetizations at  $T = 0$  K. It is easy to use the system (5), by a suitable choice of the operator  $\hat{B}$  at the right hand side of the system, i.e. with  $\hat{B} = \hat{S}_{a_1}^-$  we calculate the necessary Green's function, as

$$\begin{aligned} G_{a_1}^+(\vec{k}_{\parallel}, E) &\equiv \langle\langle \hat{S}^+(a_1) | \hat{S}^-(a_1) \rangle\rangle_{\vec{k}_{\parallel}, E} = \\ &= \frac{i}{2\pi} \frac{2\sigma_{a_1}}{\Delta(E)} \left( \frac{A_1(E_1)}{E - E_1} + \frac{A_1(E_2)}{E - E_2} + \frac{A_1(E_3)}{E - E_3} + \frac{A_1(-E_4)}{E + E_4} \right) \end{aligned} \quad (10)$$

where  $E_i \equiv E_i(\vec{k}_{\parallel})$ ,  $i = 1, 2, 3, 4$  and the corresponding coefficient

$$A_1(\pm E_i) = \left. \frac{(\pm E_i + \varepsilon_2)[(\pm E_i - \varepsilon_3)(\pm E_i - \varepsilon_4) - J_{b_1}(\vec{k}_{\parallel})J_{b_2}(\vec{k}_{\parallel})] + (\pm E_i - \varepsilon_4)\sigma_{b_1}\sigma_{b_2}J_{ab}^2}{\frac{d}{dE}\Delta(E)} \right|_{E=\pm E_i} \quad (11)$$

and

$$\Delta(E) = (E - E_1)(E - E_2)(E - E_3)(E + E_4)$$

Now using the spectral theorem, one can find the corresponding correlation function, and magnetization of the sublattice  $a_1$  in the antiferromagnetic layer:

$$\sigma_{a_1}(T) = \frac{1}{2} \frac{1}{1 + 2[\Delta\sigma_{a_1}(T) - \Delta\sigma_{a_1}^0]} \quad (12)$$

where

$$\Delta\sigma_{a_1}^0 = \frac{1}{N_{\parallel}} \sum_{\vec{k}_{\parallel}} A_1(-E_4) \quad (13)$$

i.e.

$$\Delta\sigma_{a_1}(T) = \frac{1}{N_{\parallel}} \sum_{\vec{k}_{\parallel}} \left[ \sum_{i=1}^3 \frac{A_1(E_i)}{e^{E_i/\theta} - 1} + \frac{A_1(E_4) - A_1(-E_4)}{e^{E_4/\theta} - 1} \right], \quad \theta = k_B T \quad (14)$$

where  $k_B$  is Boltzman's constant. It is important to stress here that sublattice magnetization on site  $a_1$  depends, indirectly through the coefficients  $A_1 = A_1(\sigma_{a_1}, \sigma_{a_2}, \sigma_{b_1}, \sigma_{b_2})$ , not only on the energy of elementary magnon excitation and temperature, but also on all other sublattice magnetizations in the particular system. At the temperature  $T = 0$  K, Eq. (14) vanishes so that Eq. (12) becomes:

$$\sigma_{a_1}(0) = \frac{1}{2} \frac{1}{1 - 2\Delta\sigma_{a_1}^0} \quad (15)$$

This quantity represents the quantum fluctuation of the corresponding sublattice magnetization at absolute zero. It is definitely a consequence of the given spin configuration i.e. the presence of the frustration in the system.

Following the procedure analogous to the above described one, we can determine all the necessary sublattice magnetizations. Namely, if we take the right hand side operator in the system Eq. (5) in the following order:  $\hat{B} = \hat{S}_{a_2}^-, \hat{S}_{b_1}^+, \hat{S}_{b_2}^-$  we obtain the demanded GFs and from them, by using the spectral theorem corresponding correlation functions and sublattice magnetizations.

Let us write first the magnetizations in the antiferromagnetic layers in site  $a_2$

$$\sigma_{a_2}(T) = -\frac{1}{2} \frac{1}{1 - 2[\Delta\sigma_{a_2}(T) - \Delta\sigma_{a_2}^0]} \quad (16)$$

In the ferromagnetic layers the corresponding sublattice magnetizations are

$$\sigma_{b_i}(T) = \frac{1}{2} \frac{1}{1 + 2[\Delta\sigma_{b_i}(T) - \Delta\sigma_{b_i}^0]}, \quad i = 1, 2 \quad (17)$$

Following notation was introduced in the above equations (16) and (17)

$$\Delta\sigma_{a_2}^0 = \frac{1}{N_{\parallel}} \sum_{\vec{k}_{\parallel}} A_2(-E_4) \quad (18)$$

and

$$\Delta\sigma_{a_2}(T) = \frac{1}{N_{\parallel}} \sum_{\vec{k}_{\parallel}} \left[ \sum_{j=1}^3 \frac{A_2(E_j)}{e^{E_j/\theta} - 1} + \frac{A_2(E_4) - A_2(-E_4)}{e^{E_4/\theta} - 1} \right] \quad (19)$$

where

$$A_2(\pm E_i) = \frac{(\pm E_i - \varepsilon_1)[-(\pm E_i - \varepsilon_3)(\pm E_i - \varepsilon_4) + J_{b_1}(\vec{k}_{\parallel})J_{b_2}(\vec{k}_{\parallel})] + (\pm E_i - \varepsilon_3)\sigma_{a_1}\sigma_{b_2}J_{ab}^2}{\frac{d}{dE}\Delta(E)} \Big|_{E=\pm E_i} \quad (20)$$

and

$$\Delta\sigma_{b_i}^0 = \frac{1}{N_{\parallel}} \sum_{\vec{k}_{\parallel}} B_i(-E_4), \quad i = 1, 2 \quad (21)$$

$$\Delta\sigma_{b_i}(T) = \frac{1}{N_{\parallel}} \sum_{\vec{k}_{\parallel}} \left[ \sum_{j=1}^3 \frac{B_i(E_j)}{e^{E_j/\theta} - 1} + \frac{B_i(E_4) - B_i(-E_4)}{e^{E_4/\theta} - 1} \right], \quad i = 1, 2 \quad (22)$$

where

$$B_1(\pm E_i) = \frac{(\pm E_i - \varepsilon_4)[(\pm E_i - \varepsilon_1)(\pm E_i + \varepsilon_2) + J_{b_1}(\vec{k}_{\parallel})J_{b_2}(\vec{k}_{\parallel})] - (\pm E_i + \varepsilon_2)\sigma_{a_1}\sigma_{b_2}J_{ab}^2}{\frac{d}{dE}\Delta(E)} \Big|_{E=\pm E_i} \quad (23)$$

$$B_2(\pm E_i) = \frac{(\pm E_i - \varepsilon_3)[(\pm E_i - \varepsilon_1)(\pm E_i + \varepsilon_2) + J_{a_1}(\vec{k}_{\parallel})J_{a_2}(\vec{k}_{\parallel})] + (\pm E_i - \varepsilon_1)\sigma_{a_2}\sigma_{b_1}J_{ab}^2}{\frac{d}{dE}\Delta(E)} \Big|_{E=\pm E_i} \quad (24)$$

At the temperature  $T = 0$  Eqs. (16) and (17) are given by

$$\sigma_{a_2}(0) = -\frac{1}{2} \frac{1}{1 + 2\Delta\sigma_{a_2}^0} \quad (25)$$

and

$$\sigma_{b_i}(0) = \frac{1}{2} \frac{1}{1 - 2\Delta\sigma_{b_i}^0}, \quad i = 1, 2 \quad (26)$$

System of Eqs. (25) and (26) defines the quantum spin fluctuations of magnetization in the corresponding sublattices. Let us note that the expressions for sublattice magnetizations (17) in the ferromagnetic layers are different, without any symmetry which is related to the spin configuration in the system.

We now analyze the energy of elementary excitations of the systems. We have already stressed that each energy depends on all four sublattice magnetizations so that Equation (9) must be solved numerically together with expressions for magnetizations given above.

Using such self-consistent procedure we have numerically analyzed this system of equations in the particular case of vanishing external field ( $\mathcal{H} = 0$ ) and obtained three positive and one negative branch. The results of our numerical analysis of magnon spectrum are represented in Figure 2. It should be noted that in Figure 2, according to our paper [4], we have presented all four positive branches. The needed positive branch was obtained by solving the corresponding conjugated system of equations for GFs. As for the magnetization calculation, it was determined by using only one system for GFs. The occurrence of the excitation energies, which are, of course positive, *per definitionem*, with a minus sign (we have chosen it to be  $E_4$ ) leads, after suitable algebraic manipulations, to quantum spin fluctuations in our frustrated system. System parameters used in the calculations are listed in the caption of Figure 2.

In the particular case of the absence of spin-anisotropy in the systems, i.e.  $D_a = D_b = D_{ab} = 0$ , by analyzing the free term in Eq. (9) we demonstrated the existence of the Goldstone mode (for  $k_{\parallel} \rightarrow 0$ ,  $E \rightarrow 0$ ), which in a sense confirms the correctness of our calculations.

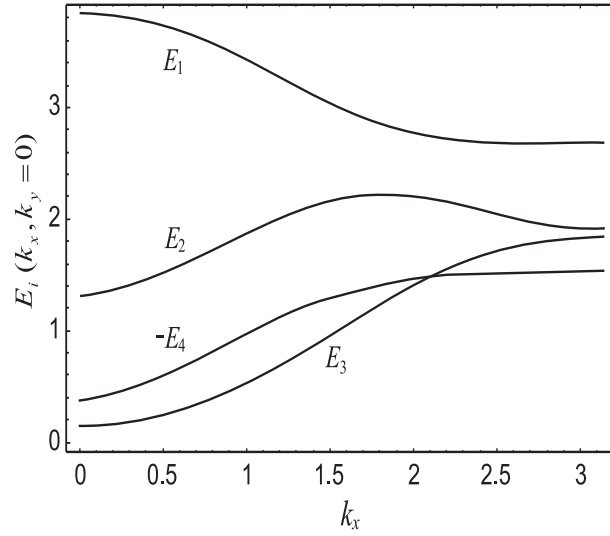


**Figure 2.** Magnon spin-wave dispersion  $E$  versus  $k_x, k_y = 0$ , with  $J_b = 1$ ,  $D_a = 0.1$ ,  $D_b = 0.1$ , and  $D_{ab} = 0.1$  at  $T = 0$  K (all quantities in units of  $J_a$ ).

Finally, it should be noted that we obtained the magnon energies and corresponding four-sublattice magnetizations in magnetic bilayer within RPA in the whole temperature range in the ordered phase. Another important characteristic of the system is the Neel temperature which remains to be determined together with other thermodynamic characteristics of these systems as the objects of our further research.

#### 4. Conclusion

To conclude, we summarize the main results obtained within the our approach.

We have applied the technique of double-time, temperature-dependent Green's functions to the magnetic bilayer described by the Heisenberg model with the XXZ spin anisotropy and spin  $S = 1/2$ . We have derived within random phase (Tyablikov's) approximation the energy of elementary excitations, four sublattice magnetizations and the corresponding quantum spin fluctuations of the bilayer in terms of the temperature. The results obtained are valid in the whole temperature range in ordered phase. Choosing a set of parameters for the model Hamiltonian, for the given temperature, we studied the energy and obtained four positive branches, as presented in the Fig. 2. Our results indicate that the exchange couplings  $J_{ab}$  and  $J_b$  play an important role in the balance and magnitude of the quantum fluctuations.

Since the studies of frustrated systems have been rather actualized recently, we plan to determine the critical temperature in these systems and study the critical exponents and other thermodynamic characteristics. Some other spin configurations at square lattices will also be the subject of our further studies.

#### Acknowledgments

This work was supported by the Serbian Ministry of Science, Technology and Environmental Protection: Grant No. 141018.

## References

1. M. G. Cottam and D. R. Tilley: Introduction to Surface and Superlattice Excitations, Cambridge Univ.Press, Cambridge (1989).
2. A. Singh, Z. Tesanovic, H. Tang, G. Xiao, C.L. Chien and J.C. Walker, Phys. Rev. Lett., **64**, 2571 (1990).
3. P. Fröbrich, P.J. Kuntz, Physics Reports, **432**, 223 (2006).
4. M. Pantić, M. Škrinjar and D. Kapor, Physica A **387**, 5786 (2008).
5. D. Kapor, M. Pantić, M. Manojlović, M. Škrinjar, S. Stojanović and M. Pavkov, J. Phys. Chem. Sol. **67**, 698 (2006).
6. D. Kapor, M. Pantić, M. Škrinjar, M. Pavkov, S. Radošević and M. Rutonjski, Phys. Stat. Sol. (b) **244**, 3750 (2007).
7. D. Kapor, M. Pavkov, M. Manojlović, M. Pantić, M. Škrinjar and S. Stojanović, Phys. Stat. Sol. (b) **241**, 401 (2004).
8. H. Diep, Phys. Rev. B **40**, 4818 (1989).
9. C.M. Soukoulis, S. Datta and Y.H. Lee, Phys. Rev. B **44**, 446 (1991).
10. A. Du and G.Z. Wei, Phys. Rev. B **46**, 8614 (1992).
11. J.G. LePage and D.R. Camley, Phys. Rev. Lett. **65**, 1152 (1990).
12. R.E. Camley and D.R. Tilley, Phys. Rev. B **37**, 3413 (1988).
13. V.Yu. Irkhin, A.A. Katanin and M.I. Katsnelson, J. Magn. Magn. Mater. **164**, 66 (1996).
14. H. Diep, Phys. Rev. B **43**, 8509 (1991).
15. A. Moschel, K. D. Usadel and A. Hucht, Phys. Rev. B **47**, 8676 (1993).
16. Wei Jiang, An-Bang Guo, Bao-Dong Bai and Guo-Zhu Wei, Physica A **384**, 377 (2007).
17. Wei Jiang, An-Bang Guo and Guo-Zhu Wei, Phys. Stat. Sol. (b) **244**, 3768 (2007).
18. N. Mermin and H. Wagner, Phys. Rev. Lett. **17**, 1133 (1966).
19. S. V. Tyablikov, The Methods in the Quantum Theory of Magnetism, Plenum Press, New York, 1967.

## Phase Sequences of Mixtures Formed by Bell-shaped and Calamitic Compounds

D. Ž. Obadović<sup>1</sup>, A. Vajda<sup>2</sup>, A. Jáklí<sup>3</sup>, M. Kohout<sup>4</sup>, M. Stojanović<sup>1</sup>, N. Éber<sup>2</sup>,  
K. Fodor-Csorba<sup>2</sup> and G. Galli<sup>5</sup>

<sup>1</sup>*Department of Physics, Faculty of Sciences, University of Novi Sad,  
Trg D. Obradovica 4, Novi Sad, Serbia ,*

<sup>2</sup>*Research Institute for Solid State Physics and Optics, Hungarian Academy of Sciences  
H-1525 Budapest, P.O. Box 49, Hungary,*

<sup>3</sup>*Liquid Crystal Institute and Chemical Physics interdisciplinary Program,  
Kent State University, Kent, OH 44242, USA,*

<sup>4</sup>*Institute of Chemical Technology, Technická 5, 166 28 Prague 6, Czech Republic,*

<sup>5</sup>*Dipartimento di Chimica e Chimica Industriale, Università di Pisa, 56126 Pisa, Italy*

Received: December 3, 2008

### Abstract

We have studied the miscibility of a non-mesomorphic bent-core molecule of new chemical architecture (bell-shape) with a polymorphic rod-like liquid crystal. Mesomorphic properties of their binary mixtures have been tested by polarizing microscopy and some structural parameters were determined using X-ray diffraction. It has been found that the mesophases exhibited by the calamitic component are preserved in certain concentration range only.

*Key words:* Bent-core compounds, liquid crystals, X-ray diffraction, molecular parameters

## 1. Introduction

Compounds with bent-core (banana-shaped) molecular architecture [1] represent a new class of non-conventional thermotropic liquid crystals exhibiting occasionally mesomorphic properties different from those of classical mesogens formed by calamitic (rod-like) or disk-like molecules [2, 3]. They have intensively been studied in the last decade [4-6] since ferroelectric switching had first been observed in an achiral Schiffs base banana compound exhibiting rich polymorphism [7]. Investigations have aimed at designing compounds with higher chemical stability (e.g. of ester type [2, 8]), lower mesomorphic temperature range and exotic phases.

Mixing compounds with different molecular structure has been proven a useful tool for adjusting phase ranges and physical properties of liquid crystals. Miscibility studies among bent-core compounds are, nevertheless, not yet as common as among calamitic liquid crystals. Though earlier trials have indicated only limited miscibility of banana

compounds, mixing bent-core molecules with calamitic ones have resulted recently in successful extension of the mesophases toward lower temperatures [9].

In search for novel mesomorphic architectures a new bell-shaped compound 5-(9-decenyloxy-carbonyl)-1,3-phenylene bis(4-nonyloxy biphenyl) carboxylate (**I**) has been synthesized. Its chemical structure is shown in Figure 1; details of the synthesis will be given elsewhere [10].

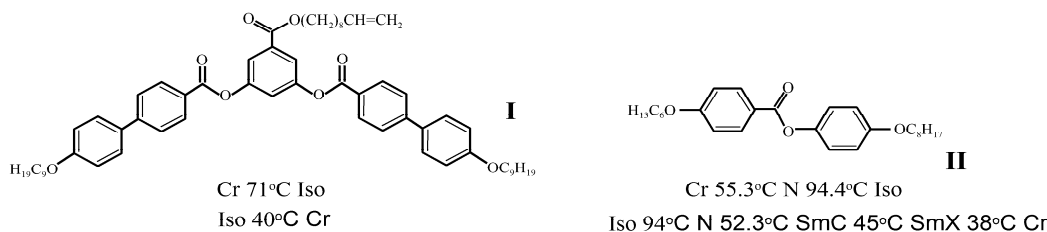


**Figure 1.** General formula of the studied materials: **I** bell-shaped compound, **II** rod-like molecule.

Although the compound has no mesophases, it exhibits low melting and freezing points. These properties have prompted us to test this compound as a component of binary mixtures. In the present paper we report on miscibility studies of compound **I** with a calamitic liquid crystal 4-(n-octyloxy)phenyl-4-(n-hexyloxy)-benzoate [8] (**II**), which exhibits an enantiotropic nematic (N) as well as two monotropic smectic (SmC and SmX) phases. The chemical structure and the phase sequence of compound **II** is also depicted in Figure 1.

## 2. Experimental

Investigations were carried out by complementary experimental techniques: polarizing optical microscopy and X-ray diffraction. For the optical studies a polarizing microscope Amplival Pol-U was used. The temperature of the samples was controlled with a Boetius hot-stage. Miscibility was first roughly checked by contact preparations; then binary mixtures of selected composition were investigated in more detail. Phase sequences and phase transitions temperatures were determined via the temperature variation of characteristic textures observed and recorded by a CCD camera attached to the microscope. Occasionally planar oriented sandwich cells with ITO electrodes were also used to check the electro-optical responses.

In order to obtain information on the structure and thus help the identification of mesophases X-ray diffraction was also performed on the mixtures. For these studies non-oriented samples were measured in transmission geometry using a conventional powder diffractometer, Seifert V-14, equipped with an automatic high temperature kit Paar HTK-10. Transmission measurements were carried out at  $CuK_{\alpha}$  radiation of 0.154 nm.

## 3. Results and discussion

The aim of the studies presented here was to understand the miscibility of bell-shaped molecules with rod-like ones and explore the mesomorphic properties of their binary mixtures. The studies were carried out on the pure compounds and on five mixtures (**Mix1**, ,

**Mix5**) with different concentrations (8.5 %, 20 %, 41 %, 50 % and 67 % by weight, respectively) of the bell-shaped compound **I**. Results of the polarizing microscopy observations are summarized in the phase diagram in Figure 2 which shows how the phase sequence of the mixtures varies with the concentration of the ingredients. As the pure calamitic compound **II** has monotropic mesophases, the data presented in Figure 2 were measured during cooling slowly from the isotropic phase.

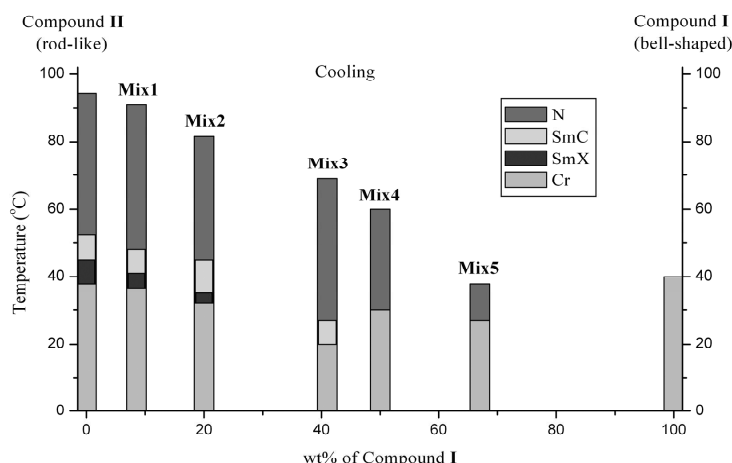


**Figure 2.** Phase diagram for binary mixtures of rod-like and bell-shaped molecules.

It is seen that the clearing point decreases with increasing concentration of the bell-shaped component which might be attributed to the low melting point of compound **I**. This is accompanied with a reduction of the width of the nematic temperature range which is not surprising as compound **I** is non-mesogenic. A similar tendency can also be observed in the N-SmC and SmC-SmX phase transition temperatures. The SmX phase disappears for concentrations of bell-shaped molecules higher than 20 wt%, while above 40 wt% even the SmC phase does not exist. It has to be noted that both smectic phases are monotropic in the mixtures just as in the pure compound **II**.

X-ray diffraction studies were carried out both on the calamitic compound and on the prepared binary mixtures which exhibited mesophases. Characteristic diffraction profiles of various phases are presented in Figures 3a for compound **II** and in 3b for **Mix1**. Analyzing the dependence of the diffraction intensities on the scattering angle  $2\theta$  the layer spacing  $d$  could be calculated from the position of the small angle diffraction peak using Bragg's law:  $n = 2d \sin \theta$ . Analogously, the average intermolecular distance  $D$  between neighbouring molecules (in a direction perpendicular to the long axes) could also be obtained from the position of the large angle diffraction peak [11, 12]. These results are summarized in Table 1. The parameters  $d$  and  $D$  were calculated with an error of  $\delta_d \approx \pm 0.1 \text{ \AA}$  and  $\delta_D \approx \pm 0.2 \text{ \AA}$ , respectively.

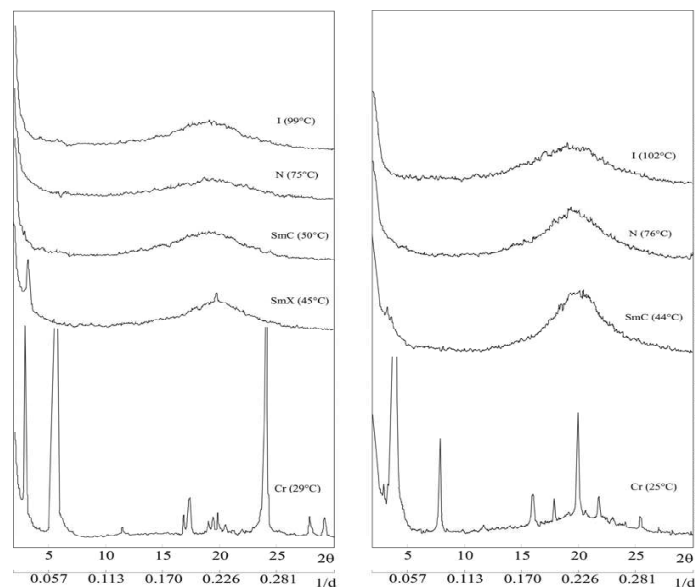


**Figure 3.** X-ray diffraction profiles for:  
 (a) rod like molecule **II**, (b) mixture **Mix1**.

The layer structure in the SmC phase of compound **II** is characterized by one reflection at a small angle  $2\theta = 3.1^\circ$ . In mixtures **Mix1** and **Mix2**, similarly, one reflection peak could be found at small angles at the same position as for the rod-like molecule, indicating the presence of the SmC phase.

**Table 1.** Molecular parameters of the investigated mixtures for all observed phases.

Mixture	T ( $^\circ\text{C}$ )	$2\theta$ ( $^\circ$ )	$d$ (nm)	$D$ (nm)
<b>II</b> (0 % of <b>I</b> )	99 (Iso)	1.91		0.464
	76 (N)	1.94		0.457
	50 (SmC)	0.31	2.845	0.448
		1.98		0.448
	43 (SmX)	0.33	2.674	0.450
		1.97		0.450
<b>Mix1</b> (8.5 % of <b>I</b> )	102 (Iso)	1.89		0.469
	76 (N)	1.91		0.464
	44 (SmC)	0.31	2.845	0.441
		2.01		0.441
<b>Mix2</b> (20 % of <b>I</b> )	106 (Iso)	1.87		0.474
	76 (N)	1.89		0.469
	53 (SmC)	0.32	2.845	0.439
		2.02		0.439
<b>Mix3</b> (41% of <b>I</b> )	79 (Iso)	1.96		0.452
	59 (N)	1.94		0.457
<b>Mix4</b> (50% of <b>I</b> )	68 (Iso)	1.92		4.62
	35 (N)	2.02		0.439
<b>Mix5</b> (67 % of <b>I</b> )	53 (Iso)	1.96		0.452
	35 (N)	2.01		0.441

This result is in agreement with the phase diagram in Figure 2, obtained from texture observations and is also confirmed by measuring the temperature dependence of the integrated transmitted intensity at crossed polarizers in oriented cells of fixed thickness (Figure 4).

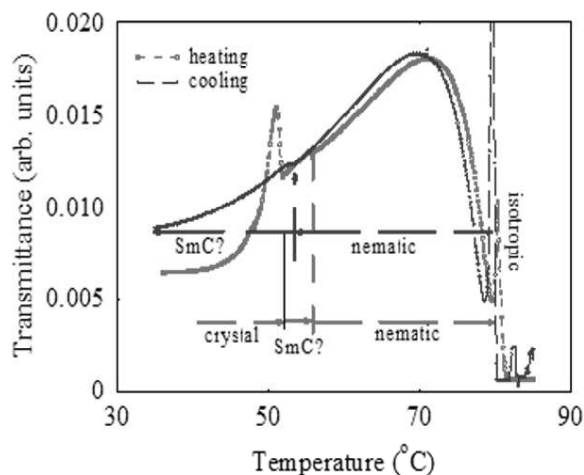


**Figure 4.** Temperature dependence of the integrated transmitted intensity for **Mix2**.

Here the small jump on the curve seen at  $55.5^{\circ}\text{C}$  on heating and at  $53^{\circ}\text{C}$  in cooling indicates the N-SmC transition. In case of the other mixtures (**Mix3** - **Mix5**) the SmC phase could not be detected and crystallization occurred directly from the N phase. The X-ray data indicate coexistence of two crystalline modifications in all investigated mixtures.

In the case of the rod-like compound **II** in the SmX phase an additional reflection was found at  $2\theta \sim 19.7^{\circ}$  which is superimposed on the broad diffusion peak (which appears in the range of  $2\theta = 12^{\circ} - 26^{\circ}$ ). This suggests the appearance of positional order within the smectic layer. Since the layer spacing in the SmX phase is smaller than in the SmC one can conclude that the SmX is also a tilted phase. Analogous reflection peak superposed on the broad diffusion peak did not show up in any of the investigated mixtures down to room temperatures, only some crystalline modifications could be identified. Thus the X-ray measurements could not justify the appearance of the SmX phase in **Mix1** or **Mix2**, in contrast to polarizing microscopy observations.

### 3. Conclusions

The present studies aimed to explore the miscibility of a non-mesomorphic bell-shaped bent-core molecule with a polymorphic rod-like liquid crystal via studying mesomorphic properties of their binary mixtures by polarizing microscopy and X-ray diffraction. Both methods confirmed that the enantiotropic nematic phase was preserved in all mixtures (i.e. up to 67 wt% of the bell-shaped compound) with gradual decreasing of the clearing point and of the width of the nematic range, while upon cooling a monotropic smectic C phase occurred only in **Mix1** and **Mix2**. By polarizing microscopy at slow cooling SmC was seen in addition in **Mix3**, and the monotropic SmX could be observed in **Mix1** and

**Mix2.** This difference between the two methods might be attributed to the fact that the phases in question are monotropic and their ability for supercooling (i.e. the temperature for crystallization) may depend on the experimental conditions (sample geometry, cooling rate, etc.). The X-ray diffraction studies of non-oriented samples have shown that all the time the SmC phase is present in the mixtures the layer spacing ( $d$ ) remains unaltered when increasing the  $wt\%$  of the bell-shaped compound.

### Acknowledgments

This work has been supported by Grant No. 141020 from the Ministry of Science and Environmental Protection of the Republic of Serbia, the Hungarian Research Funds OTKA K61075, the ESF-COST D35 WG-13/05, the SASA-HAS bilateral scientific exchange project #2, Czech-Hungarian bilateral exchange, Grants No. 202/03/P011, No. 202/05/0431 from the Grant Agency of the Czech Republic and No. 1P04OCD14.60 from the Ministry of Education, Youth & Sports of the Czech Republic.

### References

1. T. Niori, T. Sekine, J. Watanabe, T. Furukawa and H. Takezoe, *J. Mater. Chem.* **6**, 1231-1233 (1996).
2. K. Fodor-Csorba, A. Vajda, G. Galli, A. Jákli and D. Demus, *Macromol. Chem. Phys.* **203**, 1556-1563 (2002).
3. A. Jákli, S. Rauch, D. Löttsch and G. Heppke, *Phys. Rev. E* **57**, 6737-6740 (1998).
4. A. Jákli, D. Krueker, H. Sawade and G. Heppke, *Phys. Rev. Lett.* **86**, (25), 5715-5718 (2001).
5. F. Goc, Ch. Selbmann, S. Rauch, G. Heppke and R. Dabrowski, *Mol. Cryst. Liq. Cryst.* **439**, 147 (2005).
6. V. Kozmík, M. Kuchař, J. Svoboda, V. Novotná, M. Glogarová, U. Baumeister, S. Diele and G. Pelzl, *Liq. Cryst.*, **32**, 1151-1160 (2005).
7. G. Pelzl, S. Diele and W. Weissflog, *Adv. Mater.* **11**, 707-711 (1999)
8. D. Demus, H. Demus and H. Zschke, *Flüssige Kristalle in Tabellen* (VEB Deutscher Verlag für Grundstoffindustrie, Leipzig, 1974).
9. G.G. Nair, C.A. Bailey, S. Taushanoff, K. Fodor-Csorba, A. Vajda, Z. Varga, A. Bóta and A. Jákli, *Adv. Mater.* **20**, 3138-3142 (2008).
10. M. Kohout, A. Vajda, J. Svoboda, K. Fodor-Csorba and G. Galli, to be published .
11. M. Garić, A. Bubnov, M. Kašpar, V. Hamplová, V. Novotná, D.Z. Obadović and M. Glogarová, *Liquid Crystals* **32**, 565-572 (2005).
12. D.Ž. Obadović, A. Vajda, M. Garić, A. Bubnov, V. Hamplová, M. Kašpar and K. Fodor-Csorba, *J. Thermal Anal. and Calorimetry* **82**, 519-523 (2005).

*Letter to the Editor*

## On the Nuclear Two-neutrino Decay

I. V. Aničin

*Faculty of Physics, University of Belgrade, 11001 Belgrade, P.O. Box 368, Serbia*  
*e-mail: anicin@ff.bg.ac.yu*

Received: February 12, 2008

### Abstract

It is suggested that each excited nuclear state, apart from the electromagnetic decay modes, should have a very small branching ratio for the difficult to observe decay via the weak neutral current interaction resulting in the emission of the neutrino-antineutrino pair, of any flavor allowed by mass-energy considerations. Probability of the decay is estimated, and potential significance to our understanding of the neutrino is briefly discussed.

*Key words:* Weak interaction; nuclear decays; neutrino physics

*PACS number:* 23.40.Bw

### 1. Introduction

Elementary considerations suggest that the weak neutral current interaction should manifest itself not only in the interactions of free elementary particles but also in all bound systems of particles, in particular in atomic nuclei, where it should provide for yet another decay channel of excited nuclear states. The fact that this weak decay mode has up to now been neither suspected nor observed, and that it will be very difficult to observe in the future, is firstly due to its low probability and secondly due to its difficult to observe signature.

At lower excitation energies the only possibility for such a process is to run via the decay of the virtual neutral  $Z^0$  boson into the real neutrino-antineutrino pair, of any flavor that is allowed by mass-energy considerations. If the neutrino of a given flavor is different from its antineutrino (Dirac particle) the two particles can be emitted in the same state, whereas if the neutrino and antineutrino are identical (Majorana particle) they cannot be emitted in the same state. Adding to the neutrinoless double beta decay, this would, at least in principle, allow the discrimination between the two possibilities. In any case this is what we call the two-neutrino decay. If the mass composition of any neutrino flavor is such as to prevent its emission in a given transition, and if the branching ratio for the two-neutrino decay could be measured, this would, again in principle, yield independent information about the masses and mixing of neutrino mass states.

The probability for the process is intrinsically of the order of the probability for the decay of the virtual charged  $W$  boson into the real electron-neutrino pair, or the common  $\beta$

-decay. However, the  $2\nu$ -decay always competes with the many orders of magnitude more probable electromagnetic decay modes and is, minding the problems with the detection of low energy neutrinos, directly observable only with great difficulty. It is at least equally difficult to observe indirectly, as the missing intensity in the balance of intensities of observable radiations from the competing decay modes, because its contributions are far below the attainable accuracy of our intensity measurements.

We shall make a quick order of magnitude estimate of the probability for this process in one typical case where the necessary data are readily available. For this purpose we have chosen the decay of the  $388\text{ keV}$  isomeric state in  $^{87}\text{Sr}$ , which is a well-known case of the cascade of beta decays that compete successfully with the electromagnetic decay (fig. 1) [1]. This succession of weak decays shares the same initial and final states with the electromagnetic and  $2\nu$  modes and effectively results in the emission of the electron neutrino-antineutrino pair. It is realized via the two conjugated charged current interactions through the real intermediate state, instead by a single neutral current interaction, which is denoted by  $2\nu$  and marked by the dashed arrow in the drawing. The  $2\nu$ -mode should here have a practically unobservable branching ratio certainly smaller than  $2.83h/5 \times 10^{10}y$  or some  $6 \times 10^{15}$ . This should be so, in spite of a somewhat higher energy and a larger phase space, because of the necessarily bigger spin difference than that for the highly forbidden beta decay of  $^{87}\text{Rb}$ , for which the  $\log ft$  value already equals 17.6.

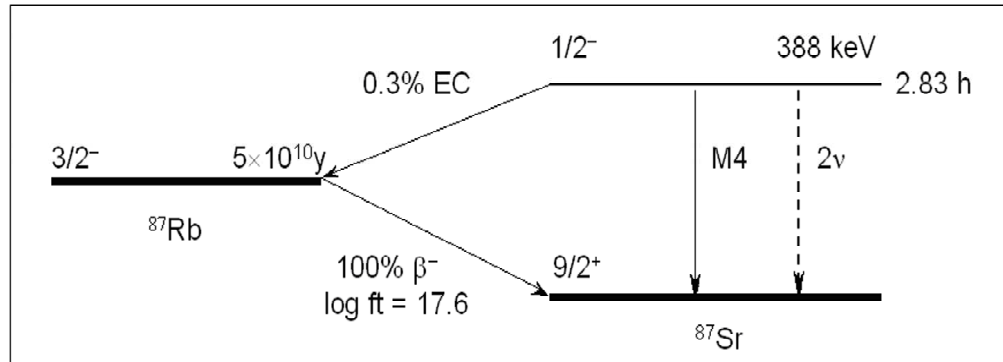


**Figure 1.** The decay scheme of  $^{87m}\text{Sr}$ , with the  $2\nu$ -decay marked by the dashed arrow.

At higher excitation energies, where the  $Z^0$  is additionally allowed to decay into the real electron-positron pair, this is masked by the electromagnetic internal pair creation of identical signature, and the contribution of this mode is perhaps even more difficult to assess than that of the two-neutrino decay.

Powerful nuclear reactors, where the processes involve a great number of excited nuclear states, mostly following the beta-minus decays of fission fragments, should have perhaps a small fraction of a watt output due to two-neutrino decays. The total neutrino flux of nuclear reactors should thus have a small component of electron neutrinos admixed to the dominating electron antineutrinos, but also an equally small admixture of muon and tau neutrinos and antineutrinos, even in the absence of neutrino oscillations. The situation with astrophysical neutrino sources is somewhat different. For instance, the spectrum of geo-neutrinos arises mostly from beta-minus decays in the radioactive series, which also involve many excited states, and should have similar relative contribution from two-neutrino decays. The processes in the sun, on the other hand, involve only light nuclei and

consequently fewer excited nuclear states. The solar neutrino spectrum should therefore contain proportionally even less neutrinos, per watt, originating from the two-neutrino decays.

To conclude, the decays of excited nuclear states via the weak neutral current interactions, and the two-neutrino decay in particular, add to the list of rare nuclear processes, the extremely difficult detection of which presents serious challenge to our experimental wits, but which in return might significantly contribute to our knowledge of the neutrino. Until then these decays, in spite of their ubiquitousness, are bound to remain just another curiosity in the nuclear zoo.

### **Acknowledgments**

The work is done as part of the Project No. 141002 “Nuclear spectroscopy and rare processes”, supported by the Ministry of Science of the Republic of Serbia.

### **References**

1. R. B. Firestone, Table of Isotopes CD ROM Eight Edition Version 1.0, p.2261 (New York, Wiley, 1996).

# Journal of Research in Physics

## INFORMATION FOR CONTRIBUTORS

This Journal is devoted to the publication of original papers in **fundamental and applied physics**. The papers are in principle Articles, while Review Articles will be published by invitation only.

Contributors should send their manuscripts to Professor M. Škrinjar, Editor, Department of Physics, Faculty of Sciences, University of Novi Sad, Trg Dositeja Obradovića 4, 21000 Novi Sad, Serbia. (Fax #: +381-(21)-459-367; E-mail: fizika@uns.ns.ac.yu).

All manuscripts must be submitted in English. Manuscripts should be submitted in duplicate and should be typewritten and double spaced with wide margins. Only one side of each sheet should be used.

Manuscripts should consist of the title, followed by author(s) name(s) and adresse(s), abstract, key words, body of the text and the list of the references. Authors should *not* include references in Abstracts.

References must be numbered in the order in which they are referred to in the text: e.g. S. Wagner [1] or [1]. In the text, such abbreviations as Ref. [4] or Refs. [7-10] may be used.

The full references should be listed in the numerical order of citation in the text at the end of the article. Examples:

1. S. Autler and C. H. Townes, Phys. Rev. A **10**, 489 (1982). – for articles
2. E. U. Shirley, *The Theory of Molecules*, p. 399, (The University Press, Cambridge, 1954). – for books
3. C. E. Moore, "Selected Tables of Atomic Spectra", NSRDS-NBS3, Setion 5, National Bureau of Standards, Washington, DC 20025 (1975). – for reports.

Tables and figures should be sent with the paper on the separate pages. All photographs, graphs, and diagrams should be numbered consecutively. The legends should be typed on a separate page at the end of the article. The author's name, the figure number, and an indication of its proper orientation should be written on the back of each figure.

Line drawings must be submitted in camera-ready form and should be drawn in india ink on stiff white paper or printed on quality laser printer. The letters and symbols should be drawn so as to be clearly legible when reduced.

Authors are asked to suggest at least three referees who may revise their manuscript.

Page proofs will be sent to the author (or the first-mentioned author in a paper of multiple authorship) for checking. **Corrections to the proofs must be restricted to printer's errors.** Authors are particularly requested to return their corrected proofs as quickly as possible. Please note that **authors are urged to check their proofs carefully before return, since late corrections cannot be guaranteed for inclusion in the printed journal.**

The first-named author of each paper will receive 25 reprints free of charge.

# Journal of Research in Physics

Volume 32    Number 1    December 2008

## CONTENTS

Perko Vukotic, Nevenka Antovic, Ranko Zekic, Ranko Svrkota and Radomir Ilic	<i>Indoor Radon Concentrations in Four Municipalities of the Central Part of Montenegro</i>	1
Miloš P. Slankamenac, Svetlana R. Lukić, Miloš Živanov	<i>Elimination of Parasitic Effects in the Measurement of Electrical Properties of High-resistance Chalcogenide Semiconductors</i>	17
A. Kapor , S. Skuban , V. Nikolić, Ž. Cvejić, S. Rakić	<i>DSC and XRD Analysis of Inclusion Complexes of Pharmacologically Active Compounds</i>	25
N. Jovančević, J. Papuga, G. Šoti, N. Todorović, J. Slivka, M. Vesković, M. Krmar, S. Forkapić, I. Bikit	<i>The Possibility of the Application of Planar Scintillation Detector for Muon Hodoscopy</i>	33
N. Jovančević, M. Dorocki, G. Šoti, D. Mrdja, N. Todorović, J. Slivka, M. Vesković, M. Krmar, S. Forkapić, J. Papuga	<i>Determination of Backscatter Effects Variation for Different Shield Materials in Low Energy Gamma Spectrometry Using Geant4 Simulation Toolkit</i>	41
S. Djurović, M. Ćirišan	<i>Asymmetry of the Central Part of <math>H_{\beta}</math> Spectral Line</i>	49
M. Pantić, D. Kapor, M. Pavkov- Hrvojević, M. Rutonjski, S. Radošević	<i>Spin-wave Theory of Frustrated Magnetic Bilayers on Square Lattice</i>	59
D. Ž. Obadović, A. Vajda, A. Jákli, M. Kohout, M. Stojanović, N. Éber, K. Fodor-Csorba and G. Galli	<i>Phase Sequences of Mixtures Formed by Bell-shaped and Calamitic Compounds</i>	69
I. V. Aničin	<i>On the Nuclear Two-neutrino Decay</i>	75